# KEKB Beam Instrumentation Systems

M. Arinaga, J. Flanagan, S. Hiramatsu, T. Ieiri, H. Ikeda,
H. Ishii, E. Kikutani , T. Mimashi, T. Mitsuhashi, H. Mizuno,
K. Mori, M. Tejima and M. Tobiyama

*KEK, High Energy Accelerator Research Organization,*
*Oho 1-1, Tsukuba, Ibaraki, 305-0801, Japan*

**Abstract**

For the stable high-luminosity operation and luminosity-increase, the electron and positron storage rings of the KEK B-Factory (KEKB) is equipped with various beam instrumentations, which have being working well since the start of the commissioning in December, 1998. Details and performance of the beam-position monitor system based on the spectrum analysis using DSPs, the turn by turn BPM with four dimensional function available for measurements of the individual bunch position, phase and intensity, the parametric beam-DCCTs designed so as to avoid the magnetic-core-selection problems for the parametric flux-modulation, the bunch by bunch feedback system indispensable to suppress the strong multibunch instabilities in KEKB, the various optical beam diagnostic systems, such as synchrotron radiation interferometers for precise beam size measurement, the tune meters, the bunch length monitors and the beam-loss monitors are described. Delicate machine tuning of KEKB is strongly supported by these instrumentaions.

*Key words:* beam monitors, beam diagnostics, storage ring, collider
*PACS:* 29.20

## 1 Introduction

In order to maintain a stable collision condition of the B-factory at KEK (KEKB), consisting of two independent storage rings [1], the high-energy ring (HER) and the low-energy ring (LER), precise beam control based on the beam instrumentations, such as beam-position monitors (BPMs), beam-size monitors and tune meters, is highly required. To realize a high luminosity on the order of $10^{34} \mathrm{cm}^{-2} \mathrm{s}^{-1}$, KEKB is operated at high beam currents with extremely many beam bunches, for example 1155 bunches in the present operation. Therefore, the beam-feedback systems used to suppress strong coupled-bunch instabilities is indispensable for the stable accelerator operation.

For measuring of the closed-orbit distortion (COD), 454 BPM-signal-pickups with 4 button electrodes are installed in the LER and 443 BPM-pickups in the HER, respectively. In order to avoid picking up the rf leakage from the high-power rf system, the 1GHz (twice the rf frequency) component of the beam-induced button signal is detected by a spectrum analysis method using a digital signal processor (DSP). The effective bandwidth of the signal detection is widely programmable, and it is easy to optimize the measuring time and the accuracy for the various operation modes of the accelerator. To ensure the reliability of a orbit measurements, the center offset of each BPM was corrected by a beam-based alignment. The CODs of both rings are continuously measured every 2–3 sec and corrected every 20–30 seconds based on the BPM data to suppress any orbit drift appearing in both rings. To keep the collision condition stable, the position offset of the interaction point and the crossing angle of electron and positron beams are automatically controlled using 4 BPMs in the interaction region. To improve the performance of the collision tuning, special BPMs with 8 button electrodes are also installed at the front end of the superconducting quadrupole magnets for the final focusing, where the positron and electron beams pass through together in BPMs. These BPMs will be in operation soon. In order to monitor the beam energy and phase miss-match in the injection process, two sets of the turn-by-turn BPMs, which detect the beam displacement and the beam phase simultaneously within one revolution time, are installed in each ring [2,3].

Interferometers of the synchrotron radiation (SR) for beam-size measurements have greatly improved the efficiency of the commissioning of KEKB. Each ring has a complete, independent synchrotron-radiation monitor. The visible SR beam, produced in a dedicated weak bending magnet for the monitor, is extracted by a water-cooled beryllium mirror and transported to an above-ground optics hutch through two parallel optical paths. One path with a relay lens system is used for direct imaging by employing a gated CCD camera; the other, without a relay lens system, is used for precise transverse beam size measurements by an SR interferometer and longitudinal bunch profile measurements by a streak camera. We developed a data-analysis method to eliminate errors caused by a surface deformation of the SR extraction mirror, and successfully improved the reliability of beam-size measurements by the SR interferometer.

Even for the usual KEKB operation, bunch-by-bunch beam feedback systems [4,5] are absolutely necessary to suppress any unexpected beam instabilities. To suppress any coupled-bunch mode of a multi-bunch instability, the frequency bandwidth of the feedback systems is required to be wider than 254 MHz, since the design goal of the bunch frequency is 509 MHz. To overcome a processing-speed problem of the digital filter, a digital processing system based on the 2-tap FIR digital filter was developed employing the custom LSIs for multiplexing/demultiplexing the data. With progress of the transverse

feedback systems, we have successfully suppressed instabilities under high-current operation and have achieved a peak luminosity of $4 \times 10^{33} \mathrm{cm}^{-2} \mathrm{s}^{-1}$ by extending the stored currents, over 900 mA in the LER and 800 mA in the HER, without any coherent beam oscillation.

In the following sections we describe the details and performance of the beam instrumentation for KEKB. The descriptions on the instrumentation related to BPMs, the bunch-by-bunch beam feedback systems, including the tune meters, and the SR monitor system are given in Sections 2, 4, 5 and 6, respectively. In Section 3, we describe the design concept and the performance of DCCTs developed for beam-current measurements of KEKB to overcome serious pairing problems of the magnetic cores for parametric flux modulation [6]. Sections 7 and 8 are devoted to the bunch-length monitors [7,8], evaluating the bunch length from the bunch spectrum, and to the beam-loss monitors, respectively.

## 2  Beam-position monitors

### 2.1  Beam-position monitors for closed-orbit measurements

The beam-position monitor (BPM) system for KEKB has been in use to measure the closed-orbit distortion since the start of commissioning in December, 1998. The HER and LER are equipped with 443 and 454 pickups, respectively. The critical elements, such as BPM signal pickups, transmission lines and electronics, were made to close tolerances. The BPM system has been regularly operating to measure the beam positions with a resolution of a few microns and a sampling period of a few seconds to correct the closed-orbit drift appearing in the KEKB rings.

### 2.1.1  Signal pickups of BPMs

A familiar type of signal pickup with four button electrodes, as shown in Fig. 1, is employed for the KEKB BPM system. To give better mechanical strength to the electrode, the button electrode is designed in a one-body structure with a large-diameter central rod of an N-type feed-through, as shown in Fig. 2. The body of the BPM pickup is made from a solid piece of copper, as is the beampipe, and four feed-throughs with electrodes are brazed onto the body. Button electrodes with normal rods are used for the pickups in the LER and for part of the HER, while the button electrodes for use in the HER arc sections are non-axially-symmetric rods based on considerations of the coupling impedance so as to avoid the growth of coupled-bunch instabilities [9].

Every BPM pickup is firmly and precisely supported at the end of a quadrupole magnet, as shown in Fig. 3. The flat surface of the stainless-steel frame brazed on the pickup body also serves as a reference plane for setting the pickup.

The KEKB rings lie about 10 m below the ground level, while the electronics system is installed in 20 sub-control buildings on the ground level. The beam signals from the four button electrodes of each BPM pickup are transmitted through independent coaxial cables with lengths of 40–150 m. To overcome possible radiation damage due to radiation, a 20 cm-long radiation-resistant PEEK (poly-ether-ether-keton) insulation cable is connected between the signal transmission cable and the feedthrough of a pickup electrode. The expected radiation dose of $7.3 \times 10^5$ rad/year for the LER or $9.1 \times 10^7$ rad/year for the HER at the connector of the button electrode is considered to be manageable by the PEEK-cable based on 1 Grad-irradiation test by $\gamma$-rays.
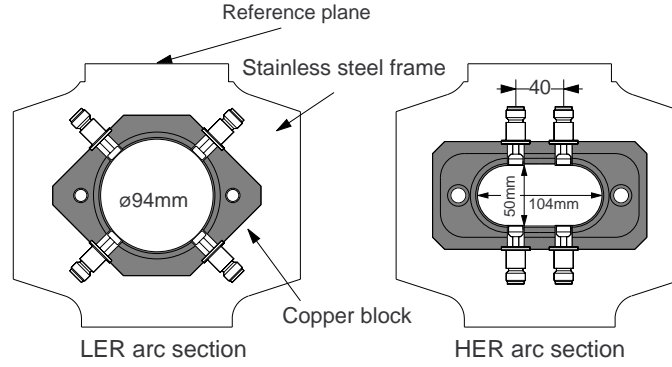

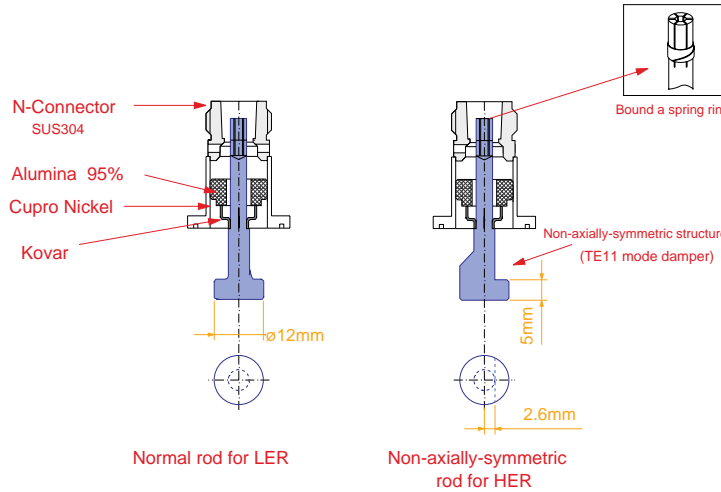
Fig. 1. BPM-signal pick-ups for KEKB.



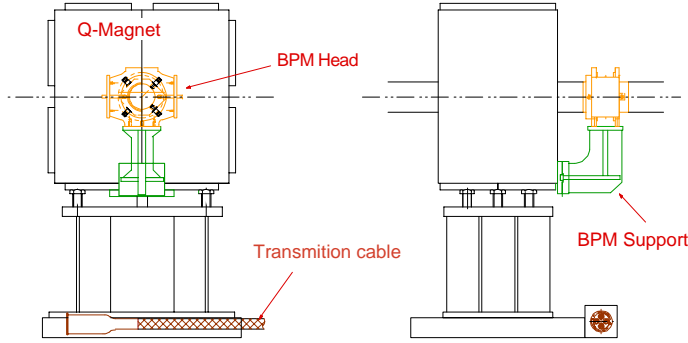Fig. 2. Button electrodes of the pickups.

4

Fig. 3. Support of a BPM pickup.

### 2.1.2  Signal processing and system layout

To avoid possible noise caused by the high-power rf system of the KEKB rings, the signal component at the 2nd harmonic frequency (1018 MHz) of the accelerating rf frequency (509 MHz) is detected using super-heterodyne circuits and spectrum analysis by means of an FFT (fast Fourier transform). The signal detection circuit consists of a super-heterodyne circuit, a 16-bit analog-to-digital converter (ADC) and a digital signal processor (DSP). Figure 4 shows a block diagram of the front-end electronics. The super-heterodyne circuit converts a picked-up signal frequency into an intermediate frequency (IF) of 20 kHz. To avoid errors related to nonlinear elements such as an envelope detector with diodes or synchronous detectors with double balanced mixers, the IF signal is digitized directly by the ADC at a 100 kHz sampling rate, and the frequency spectrum is calculated by a DSP with an FFT algorithm to obtain the required signal amplitude. The number of FFT data points, which determines the effective bandwidth of signal detection, is programmable so that it is easy to optimize the resolution of the beam-position measurement and the measuring time for the various operation modes of the KEKB rings. Furthermore, the DSP has a data averaging function to increase the S/N ratio.

The electronics units are designed based on the VXI standard and distributed in 20 local control buildings around the KEKB tunnel. Six VXI mainframes are installed in each local control building for the BPM system. Two front-end signal processors and four dual 4-channel signal multiplexers used to select the BPM-signal pickup and the button-electrode signal for the front-end electronics module are set into every VXI mainframe, as shown in Fig. 5. The digital output of the front-end processor is sent to a VXI bus of the mainframe in each local control room. Each VXI mainframe is linked directly to the VME-bus of the IOC (input/output controller) of the EPICS system, which is the control system for KEKB [10], by a high-speed MXI (multisystem extension
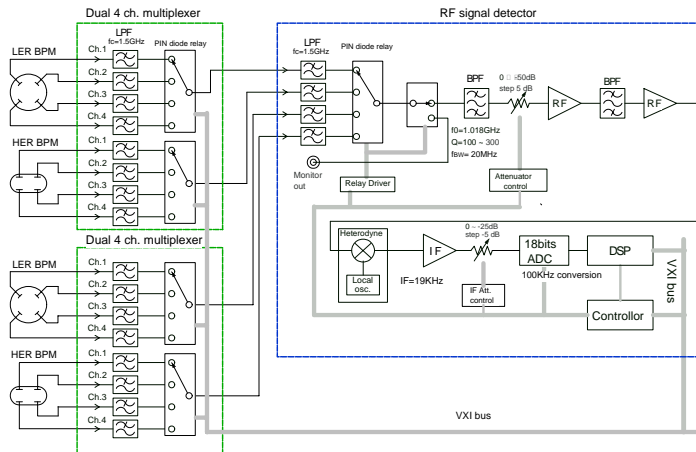
Fig. 4. Block diagram of the front-end signal processor.

interface bus). The IOC and UNIX workstations for the operator's consoles are connected through a high-speed network.
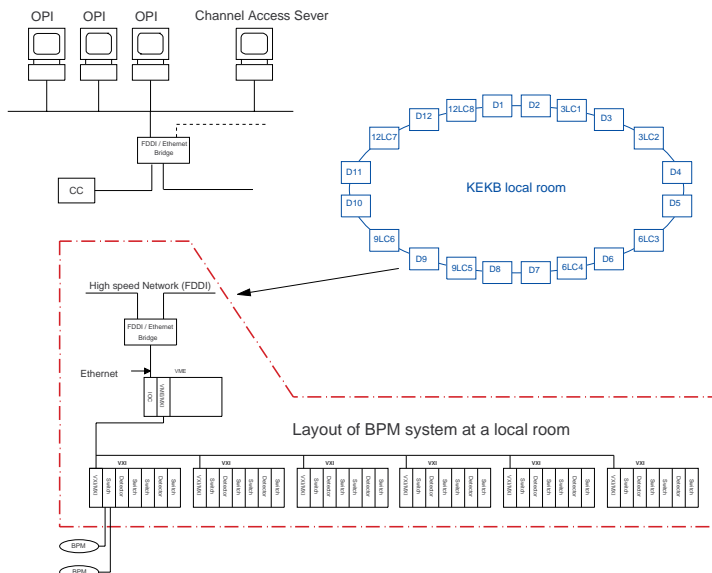


Fig. 5. Layout of the BPM control system.

### 2.1.3 Setting of BPM-pickups and beam-based alignment

The BPM-signal pickups were fabricated to within a mechanical tolerance of $\pm 0.1$ mm. However, we have non-ignorable differences in the frequency response among the four button electrodes. All BPMs were mapped at a test bench using a movable antenna to identify the electrical center of each pickup, and were calibrated to about 20 $\mu$m accuracy. Then, most BPM pickups ($\sim 97\%$) were aligned in relation to their nearest quadrupole magnets within a setting error of $50\mu$m. After installation of the BPM-pickups in the rings,

6

the mechanical offsets relative to the corresponding quadrupole magnets were measured with good reproducibility ($38\mu$m in horizontal and 16 $\mu$m in vertical directions). Finally, to correct the imbalance of the signal attenuation at 1018 MHz in the signal transmission cables and in the signal multiplexers, the cables together with the electronics were also calibrated to 50 $\mu$m accuracy with test signals applied at the front ends of four signal transmission cables.

Usually, the beam position is calculated from the signal amplitudes of the four electrodes (A, B, C and D) of a BPM-pickup. Additionally, four sets of beam-position data are also obtainable from the signal amplitudes of any three electrodes chosen out of four electrodes: (A, B, C), (B, C, D), (C, D, A) or (D, A, B). If the signal amplitudes of four button electrodes have an ideal correlation, these four beam positions should coincide with each other. The software of the BPM system calculates beam positions using not only four electrode-signals, but also three electrode-signals to examine the consistency among these position data. Almost all BPM-readings have significant differences of larger than 0.1 mm among the four positions obtained from three-electrode signals. It is considered that heating of the beampipe for de-gassing after brazing the BPM-pickup onto the beampipe caused a small imbalance of the feedthrough contacts of the button electrodes. To correct the overall errors in the BPM system, we performed a beam-based alignment, or beam-based calibration, for all BPMs in the KEKB rings. The beam-based alignment estimated the center offset of each BPM pickup from the magnetic-field center of a quadrupole magnet according to the "Quad-BPM response method" [11], where the BPM offset was determined by looking for the BPM-reading of the beam position at a quadrupole magnet that showed no-response against an intentional small change in the quadrupole field. Histograms of the measured offsets are shown in Fig. 6. These offsets are used to correct BPM-readings in the software. The rms of the measured CODs is improved from 0.4–0.5 mm without any offset correction to 0.3–0.4 mm with an offset correction, as shown in Fig. 7.

### 2.1.4 Position resolution

Figure 8 shows test-bench measurements for the resolution and the measuring time of the prototype front-end circuit module at an input level of −60dBm, corresponding to a 10 mA beam current. The results obtained at several data-sampling conditions for the FFT are plotted against the total number of data points for the FFT analysis, given by (number of FFT data points)×(number of times averaged). The resolution of the beam-position measurement is improved in proportion to the square root of the total number of data, and is consistent with the expectation from a noise analysis assuming thermionic noise at the input stage of the front-end module including the signal transmission cable. A resolution of about 0.5 $\mu$m, which corresponds to an S/N ratio of 91 dB in the detection of each button-signal, can be expected with a measur-
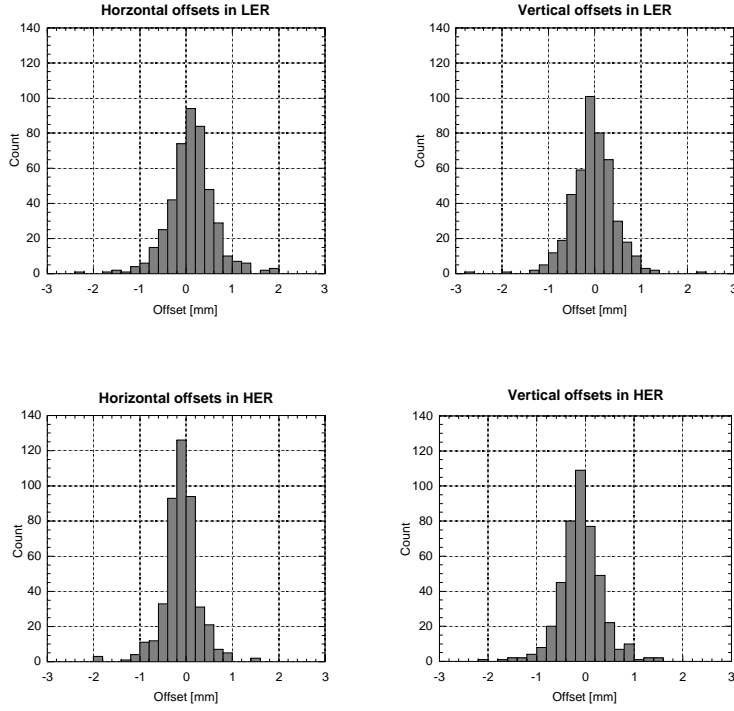
Fig. 6. Histogram of offset measured by beam based alignment in the LER and HER.
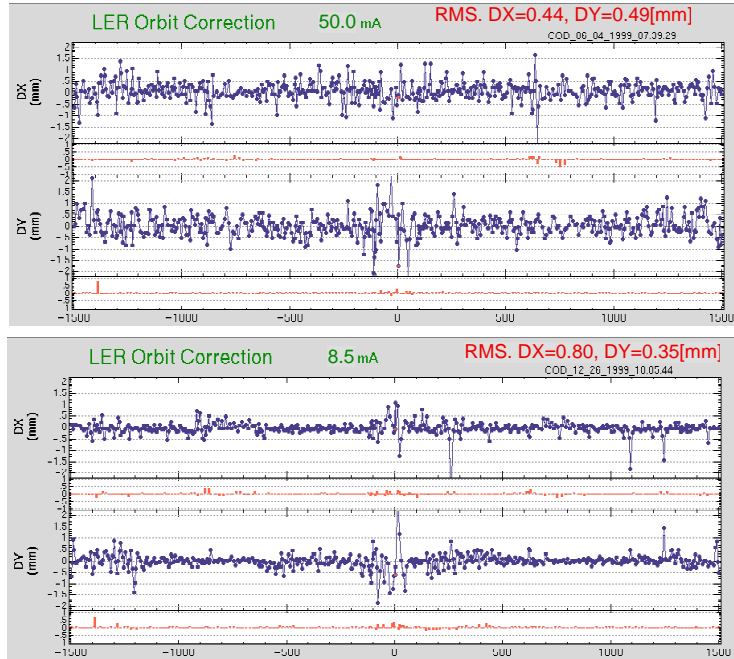


Fig. 7. Closed orbit of the LER. Upper graph is the COD before the beam-based alignment, and lower graph is that after the beam-based alignment.

ing time less of than 1 second per BPM for the beam position measurement in the LER with the DSP function of "2048-points FFT and 8-times average".
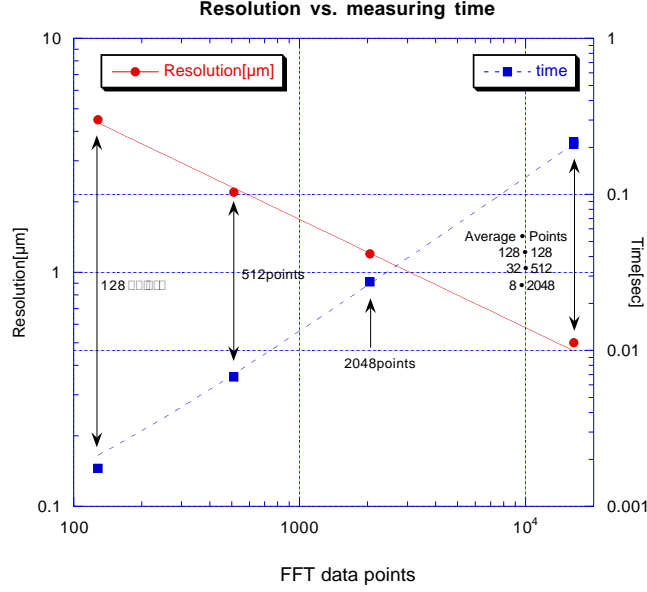
Fig. 8. Resolution and Measuring time evaluated at the test bench.

The expected resolution, $\sigma$, is given by $\sigma = K/\{2(S/N)\}$, where $K$ is the sensitivity factor determined by the BPM-pickup structure ($K = 33$ mm (horizontal and vertical) for the LER and $K = 19$mm/$28$mm (horizontal/vertical) for the HER), and S/N is the signal-to-noise ratio of the detected signal amplitude of each button electrode. To evaluate the resolution in the actual beam-signal detection, the spectrum of the beam-signal from a button electrode was taken by an FFT analysis in the DSP after completion of the BPM system. A typical example of the spectrum is shown in Fig. 9, where the S/N ratio of about 75 dB for the actual beam is obtained with the DSP function of "2048 points FFT without averaging". Applying the averaging-function of the DSP with 8-times average, an S/N ratio is expected to be improved to 84 dB, corresponding to a resolution of 0.6–1 $\mu$m, which is high enough for COD measurements, although we have a degradation of the S/N ratio by about 7 dB from the test-bench measurement. In regular operation of the BPM system, the number of data averaging is chosen to be 4 to speed up the COD measurement cycle with an expected resolution of 1.2–1.6 $\mu$m.

One of the direct measurements of the BPM-resolution is the "3-BPM correlation method" [12]. Assuming a linear correlation of $x_3 = ax_1 + bx_2$ between three beam positions $x_1$, $x_2$ and $x_3$ at three neighboring BPM locations and applying a least-squares analysis to many sets of $(x_1, x_2, x_3)$ measured by these three BPMs, we can calculate the coefficients $(a, b)$ and the correlation variance, $\sigma = \sqrt{\overline{(ax_1 + bx_2 - x_3)^2}/(1 + a^2 + b^2)}$, where $\overline{(ax_1 + bx_2 - x_3)^2}$ is the average of $(ax_1 + bx_2 - x_3)^2$. The resulting $\sigma$ is equivalent to the resolution in
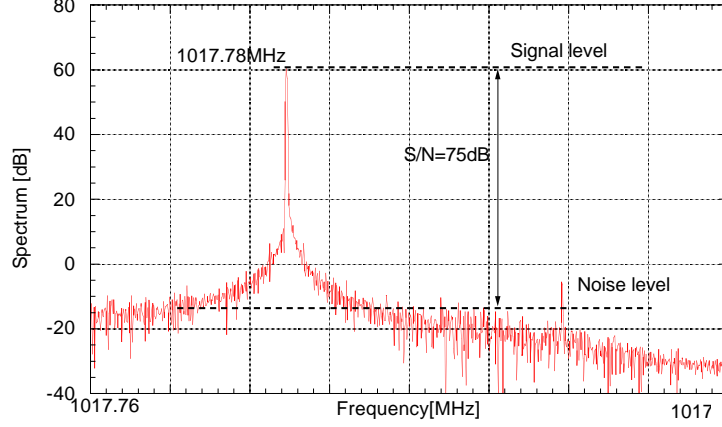
Fig. 9. Spectrum data of FFT analysis at DSP.

the detection of the beam position. By appling the 3-BPM correlation method to all BPMs around the rings, position resolutions were confirmed to be within a few $\mu$m at almost all BPMs, as shown in Fig. 10, and is consistent with the estimation from the S/N ratio. However, the horizontal-position resolution in the LER is relatively poor. This may be due to the orbit oscillations described in Section 2.1.6.
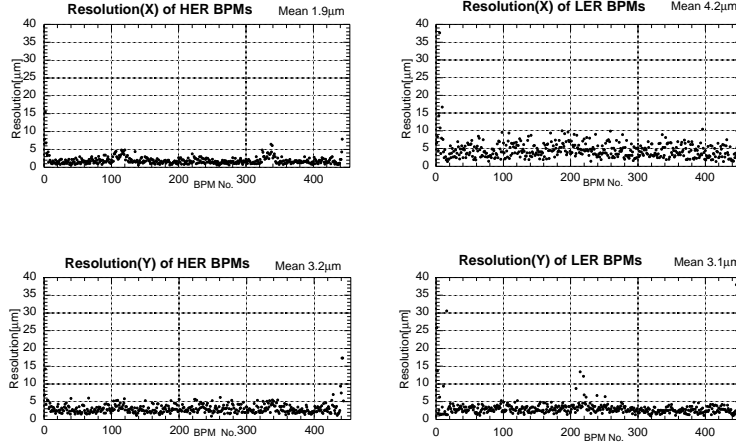


Fig. 10. Distribution of all BPM resolutions in the KEKB rings.

## 2.1.5  Measurement error due to the HOM signal

Around the interaction point, we have four BPMs with peculiar cross sections at the quadrupole magnets, QC2RE, QC3RE, QC4RE and QC2LE. The waveguide-mode cut-off frequencies of their beampipes are very close to, or slightly lower than the standard detection frequency 1018 MHz of the BPM system. The spectral components at 1018 MHz detected by BPMs at these locations are contaminated by the wake fields of higher order modes (HOMs)

10

propagating in the beampipe. In order to avoid the influence of HOMs, we changed from 1018 MHz detection to 509 MHz detection for these BPMs. Due to this change in the detection frequency, the BPM readings changed as shown in Table 1.

Table 1
Difference of the BPM-readings between 1018 MHz and 509 MHz detection.

|  | 1018MHz detection | | 508 MHz detection | |
| --- | --- | --- | --- | --- |
| Qmag. | X [mm] | Y [mm] | X [mm] | Y [mm] |
| QC4RE | −0.351 | 4.497 | −2.168 | −0.230 |
| QC3RE | 1.159 | −3.860 | −0.042 | -0.897 |
| QC2LE1 | −0.868 | 1.849 | −1.527 | −0.237 |
| QC2LE2 | 0.391 | 3.014 | −0.298 | −0.165 |

### 2.1.6   Measurement of closed-orbit oscillations

Since oscillations of the beam orbits exist in both the HER and the LER, we applied the BPM system to measurements of the oscillation amplitudes to find out the oscillation source. The BPM system is typically operated so as to measure beam positions at two second intervals. A slow variation of the closed orbit over several seconds is continuously corrected by the orbit-correction system to maintain the golden orbit. On the other hand, the BPM system enables us to measure oscillations above 1 Hz up to about 30 Hz by changing the sampling speed by means of the DSP parameter choice. By applying an FFT analysis to the accumulated data in the EPICS computer system taken by BPMs in the fast sampling mode, we can detect oscillation amplitudes within 1 $\mu$m resolution. As a typical example, Fig. 11 shows the normalized amplitude of a 0.47Hz component traced in the betatron phase advance in the neighborhood of an oscillation source in the LER [13]. The peak amplitude in this figure corresponds to about 20 $\mu$m. The high resolution of the BPM system ensures observations of such small-amplitude orbit oscillations. This result showed the oscillation source to be a 0.47Hz leakage component of the magnetic field of the nearby proton synchrotron.

### 2.2   Special BPMs for the interaction point

Two special BPMs with 8 button electrodes, called OCTPOS, are installed inside the inner bore of the superconducting magnets (QCSs) for final focusing, as shown in Fig 12. In addition to OCTPOSes, four BPMs with four button electrodes, indicated by QCS-L and QCS-R are incorporated outside of the two QCSs in order to complement the OCTPOSes. The crossing angle between
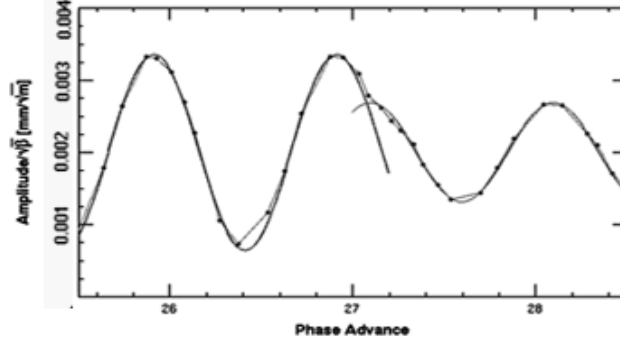
Fig. 11. Trace of the orbit oscillation amplitude of 0.47Hz component in the neighborhood of the oscillation souce.

the electron and the positron beams and the beam-beam kick angle at the IP are measured based on the beam-beam deflection technique by these special BPMs [14]. The orbit separation around the IP is so small that both beams pass together through the OCTPOSes. Although a stripline-type pickup could be used to detect each beam-signal separately, a pickup with a button electrode, i.e., OCTPOS, was chosen because of serious space constraints inside QCSs. An arithmetic manipulation of the eight button-electrode signals based on the non-linearity of the signal pickup makes it possible to separate each beam signal from the composite signal.
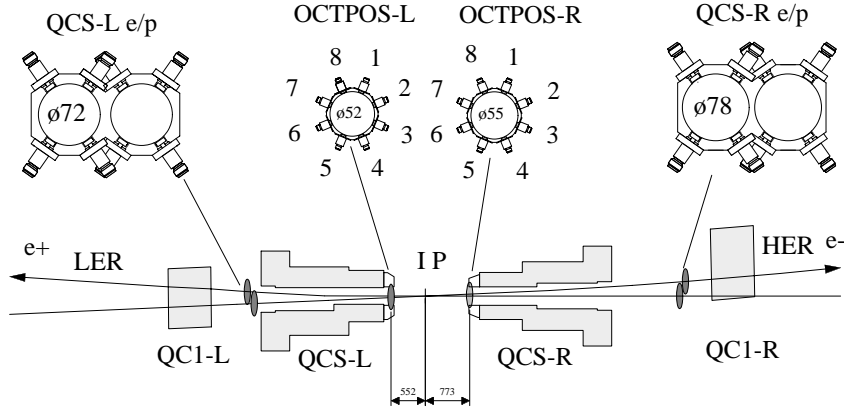


Fig. 12. Schematic view of the KEKB IR.

### 2.2.1  Signal pickups

A feedthrough with an SMA-type connector is employed for the button electrode of OCTPOS, because we have little space between the beampipe and the inner surface of the QCS bore. To avoid contact deterioration of the connector, the female contact pin of the SMA connector was changed to a male contact pin, as shown in Fig. 13. Since the BPM pickups at the exits of the QCSs (QCS-L and QCS-R) with twin-chamber structures as shown in Fig 12 are not supported firmly onto QCSs, mechanical movements of these pickups result from a temperature rise of the beampipe by beam currents, as shown in Fig. 14. These movements of the pickups are compensated in the BPM-readings automatically using of the displacement sensors in order to maintain a stable beam collision condition.
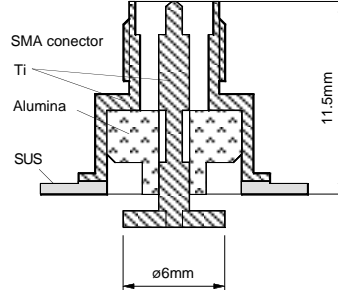


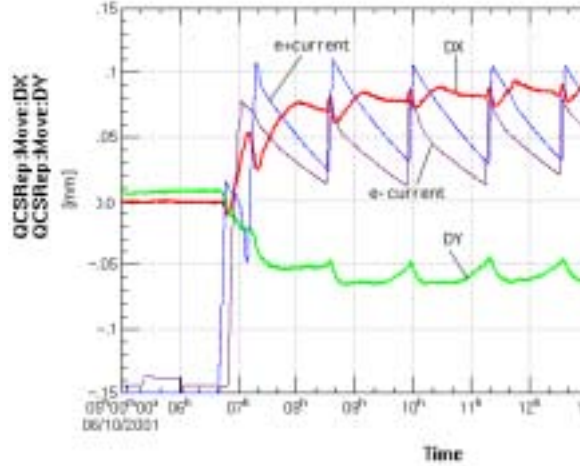Fig. 13. Button electrode for OCTPOSes.



Fig. 14. Movement of the QCSR BPM chamber and beam intensity records.

### 2.3  Beam position measurement by OCTPOSes

The eight electrode-signals of an OCTPOS are processed by the same electronics as are employed in the closed-orbit BPM system. The front-end signal

13

processor of OCTPOS detects the amplitude of the composite signal of two beams by an FFT analysis with 64 sampling points, and the average of 16 measurements is ultimately processed by the IOC controller to obtain a fast measuring cycle of OCTPOS for the feedback control of the corrector-magnets for the beam-collision tuning. A composite signal amplitude, which is a function of seven unknown quantities $(Q_e, x_e, y_e)$, $(Q_p, x_p, y_p)$ and $\theta$, gives a constraint on the relation among these unknown quantities, where $(Q_e, x_e, y_e)$ are the charge and the position of the electron beam at the BPM-pickup, $(Q_p, x_p, y_p)$ are those of the positron beam, and $\theta$ is the phase difference between the two beams. When the signal amplitudes of the eight button-electrodes of a pickup are detected simultaneously, the beam position of each beam is separable by analyzing the non-linearity of the pickup sensitivity, because the number of unknown quantities is smaller than the number of the constraints [15]. Figure 15 shows the preliminary result of an analysis concerning the actual beam measurements. In these measurements, we fixed $\theta$ to be $\pi/4$ which is the expected phase difference from the distance between the OCTPOS-pickup and the IP, since this analysis has a tiny tolerance for the error of $\theta$. We can obtain the beam positions of electrons and positrons separately, as shown in this figure. Although the OCTPOS BPM system is almost ready for use, a 3-BPM correlation analysis based on the lattice model of the ring indicates that a difference of about 10 $\mu$m exists in the analyzed beam positions in OCTPOSes between the single-beam case and the two-beam case. We need more detail investigations for the actual use of OCTPOSes for feedback control of the collision tuning.
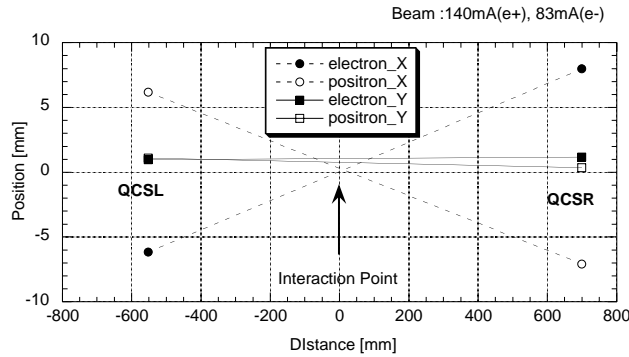


Fig. 15. Beam positions at OCTPOSes obtained from composite button-electrode signals induced by the electron and the positron beams.

## 2.4 Turn-by-turn position monitors

In addition to the BPM system for the closed-orbit measurement described in the previous section, four sets of the turn-by-turn beam-position monitors are installed in the KEKB rings. The bandwidth of the detector system is designed to be 20 MHz to select the beam signal of a specific turn. At the central part

of the detector circuit, an I/Q-demodulater (in-phase and quadrature-phase synchronous detector) consisting of two hybrids and two balanced mixers is employed to measure not only the amplitude, but also the phase of the beam signal simultaneously. The function of the system is extended to a single-bunch measurement in a bunch train using high speed rf-switches to pick up a specific bunch signal.

### 2.4.1 System and performance

Figure 16 shows a schematic diagram of the turn-by-turn beam position-monitor, representing only one channel out of four channel electronics. A beam signal detected by a button electrode of the BPM head is filtered by a band-pass filter (BPF) tuned at the rf frequency (509 MHz) of the ring with a bandwidth of 60 MHz. Although a bandwidth of several hundred kHz is enough to resolve the beam signal in turn by turn, the signal-to-noise ratio (S/N) of a transient signal, such as a beam bunch signal, is expected to be improved in proportion to the square root of the bandwidth of the detection system. Detected signal voltages in orthogonal phase by the I/Q-demodulator ($V_{\sin}$ and $V_{\cos}$ in Fig. 16) are sampled by 14-bit ADCs simultaneously, and the ADC data is stored in a memory chip with a capacity of 64 kwords mounted on the ADC board. The sample timing of the ADC is adjustable in bucket-by-bucket timing, and its repetition is programmable in the manner of $f_{rev}/N$, where $f_{rev}$ is the revolution frequency of the ring and $N$ is a programmable number from 1 to 256.
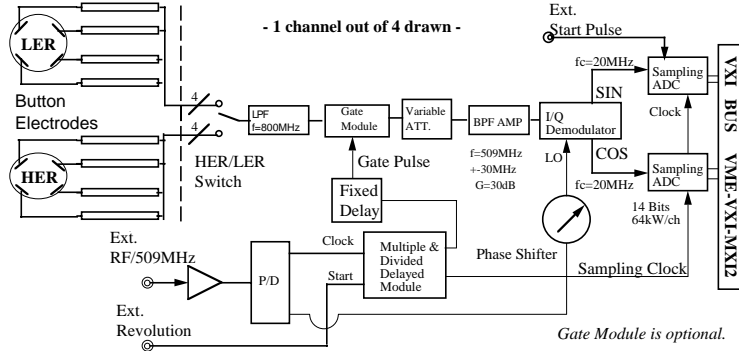


Fig. 16. Schematic turn-by-turn and bunch-by-bunch beam position monitor.

The beam signals detected by four button electrodes are processed in parallel with a bandwidth of 20 MHz by the four-channel electronics to calculate the beam position in turn-by-turn using four signal intensities, each of which is given by $V = \sqrt{V_{\sin}^2 + V_{\cos}^2}$, corresponding to each button electrode. The bunch intensity is obtained by summing up four signal intensities, and the phase difference between the beam signal and the reference rf-clock is given by $\varphi_b - \varphi_{\rm rf} = \tan^{-1}(-V_{\sin}/V_{\cos})$, where $\varphi_b$ is the beam phase and $\varphi_{\rm rf}$ is the rf phase. Since the bandwidth of the BPF is not wide enough to pick up a

15

specific bunch signal, a four-channel gate module consisting of commercially available rf-switches (Macom, SW-209) is atached in front of the detector. The rf-switch has some oscillatory behavior at the transition from on-state to off-state. Therefore, two switches are connected in series, as shown in Fig. 17, to improve the switching response, where the delay time of the gate pulse for the second switch (pulse 2 in Fig. 17) determines the gate duration. With this gate circuit, we have achieved a minimum gate duration of 6 ns with an insertion loss of 3 dB, which is available to select one bunch in a bunch train at the current operation of KEKB with an 8 ns bunch spacing (or 4 rf-bucket spacing). At present, the bunch-selection gate module is introduced only in one detector out of four for the performance test [3]. The measured on/off isolation of the gate module using an actual beam signal of the HER is shown in Fig. 18 where the detected bunch intensity in a bunch train (shown by squares) and that of a isolated bunch injected in the bunch gap (shown by dots) are plotted as a function of the gate timing. This result indicates that a specific bunch signal can be identified with a separation of more than 32 dB for the neighboring bunch in a bunch train with 4 rf-bucket spacing.
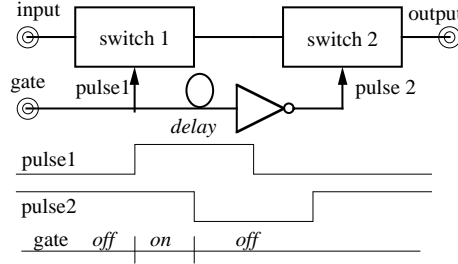


Fig. 17. Schematic diagram of the gate module for bunch selection.
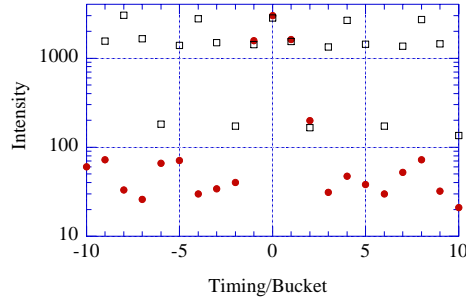


Fig. 18. Variation of intensity as a function of timing of the gate, where timing "0" is optimum. Dots are measured intensity around an isolated bunch and squares are intensity of bunches with 4-bucket spacing in a train.

The performance of the turn-by-turn BPM system is summarized in Table 2. It is expected that the turn-by-turn BPM has potentiality for detailed investigations on the beam dynamics, as described in the next section. As a next step of system improvement, it is desired that the position error caused by an imbalance between two output ports, i.e., I-port and Q-port, of the I/Q-demodulator and also the phase variation of the gate module depending on

16

the bunch intensity in the bunch phase measurement should be compensated in data processing based on a test-bench calibration.

Table 2
Summary of the obtained specifications. The figures with asterisk(*) are those specifications without the bunch selection gate module.

| System bandwidth | 20MHz |
|---|---|
| Linear range | 40dB* |
| Minimum detection level | 50pC or 5$\mu$A |
| Position resolution | 50$\mu$m @1 nC or 0.1 mA |
| Position accuracy | 0.5 mm |
| Position variation against the phase | 0.45mm/90° max |
| Phase resolution | 0.5degrees for $>$ 1nC<br>$<$ 0.1degrees with averaging |
| Memory capacity | 64,000$\times N$ turns,<br>$N$ : divide ratio of sampling pulse |
| Isolation of switch | 32dB at 3 buckets apart |

### 2.4.2  Applications

The turn-by-turn BPM system is quite useful for the beam-injection tuning, since the transverse and longitudinal oscillations of a beam bunch in addition to the bunch intensity are measured simultaneously. For example, at the first trial of beam injection into a ring without an accelerating rf-field in the first commissioning of KEKB, fine tuning of the rf frequency was performed based on a beam-phase measurement by the turn-by-turn BPM. The observed phase drift of 4 deg/turn of the injected beam bunch against the reference rf-clock required the rf frequency to be lowered by 1.1 kHz for storing the beam in the ring.

In the regular tuning of beam injection, the energy-phase mismatch between the injected beam and the ring is compensated so as to minimize the synchrotron oscillation. In Fig. 19(a) a typical example is shown for the bunch-phase oscillation just after injection with an energy mismatch, where a sine-like oscillation pattern is observed as predicted from the particle motion in longitudinal phase space. On the other hand, in Fig. 19(b) the cosine-like oscillation observed here is dominated by phase mismatch.

Excellent performance of the turn-by-turn BPM for investigations of the beam dynamics has been demonstrated in the measurement of the damping rate of betatron oscillation and in measurement of the synchronous-phase shift. The
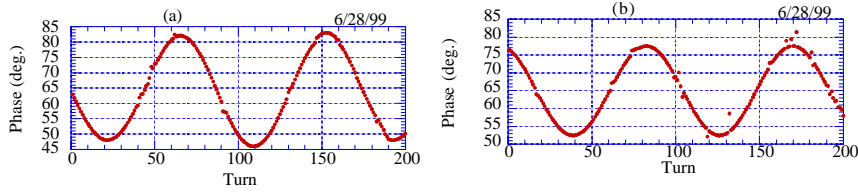
Fig. 19. Two examples of synchrotron motion of an injected beam with the rf-voltage of 8 MV in the HER.

measured vertical betatron oscillation excited by a kicker magnet is shown in Fig. 20. A damping rate of 350 sec$^{-1}$, estimated from this measurement, is much larger than the rate of 23.4 sec$^{-1}$ expected from radiation damping. This difference is caused by head-tail damping due to the ring impedance and the chromaticity.

As for a measurement of the synchronous-phase shift, $\Delta\phi_s$, we can evaluate the loss factor, $k$, caused by the resistive impedance based on an approximate expression of $k \approx (V_c \cos\phi_{s0}/T_0 I_b)\Delta\phi_s$ by measuring $\Delta\phi_s$ as a function of the bunch current, $I_b$, where $V_c$ is the rf voltage, $\phi_{s0}$ the synchronous phase and $T_0$ the revolution period. Figure 21 shows the measured synchronous phase as a function of $I_b$ in the single-bunch mode operation. It is considered that the variation of the synchronous phase observed in this measurement indicates the variation of $\Delta\phi_s$ associated with loss factors coming from some resistive impedance. It seems that the loss factor decreases steeply as the bunch current increases in the small-current region where bunch lengthening starts to grow and then gradually decreases in the high-current region.

The last example of the applications of the turn-by-turn BPM is a measurement of the phase variation caused by transient beam loading. In the multibunch-mode operation of KEKB with 1153 bunches filled at every 4th rf-bucket, the measured phase variation of an individual bunch in a bunch train is shown in Fig. 22 as a function of the bucket number. In this measurement, the intensity of every bunch is regulated within ±5% to suppress the phase error of the bunch-selection gate module within ±0.3 degrees. Transient beam loading is clearly observed. (see the paper on the rf systems in this series for details.)

A new type of beam-position monitor employing I/Q-demodulators and the bunch-selection gates enable us to detect transverse and longitudinal positions in addition to the bunch charge simultaneously in turn-by-turn and also in bunch-by-bunch. Such a four-dimensional function of this monitor is quite useful for beam injection tuning into the ring and for detailed investigations of the beam dynamics related to the coupling impedance and transient phe-
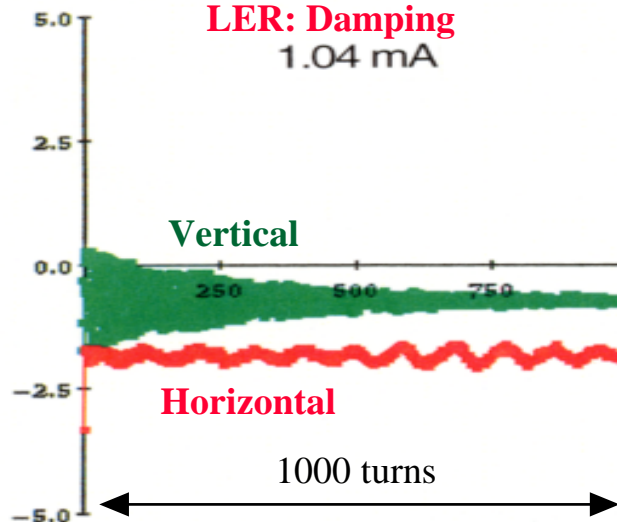
18

Fig. 20. Damping of vertical betatron oscillation in the LER, measured at the bunch current of 1.04mA with the vertical chromaticity of 1.4. The vertical scale is in mm, the horizontal is in turn.
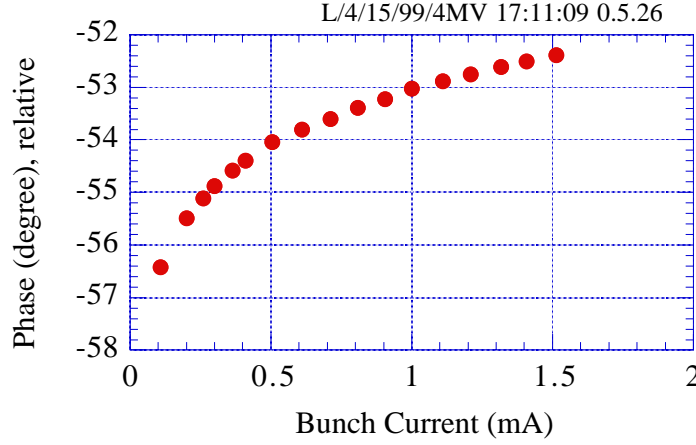


Fig. 21. Bunch phase as a function of the bunch current in the LER, the natural bunch length is 5.1 mm and the cavity voltage is 4MV.

nomena.

## 3 Direct-current transformers and current transformers

### 3.1 DCCTs

For measuring beam currents in the KEKB storage rings we developed parametric beam DCCTs with new feedback circuits, which are essentially free from parametric modulation ripple, in order to overcome the serious pairing
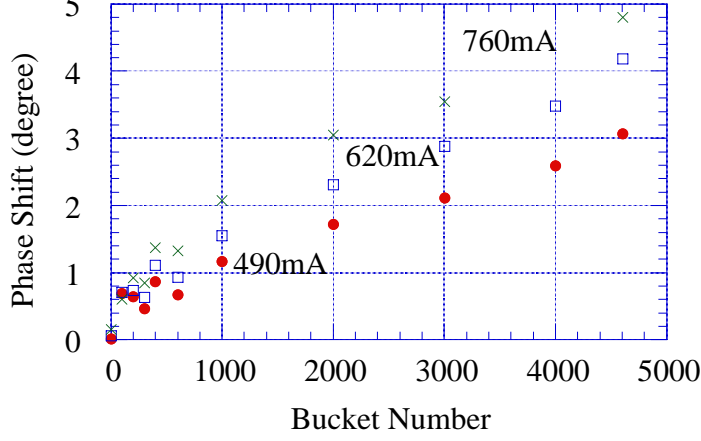
19

Fig. 22. Bunch-by-bunch phase along a train as a function of the bucket number measured with the total cavity voltage of 11MV in the HER. The phase is plotted for the beam current of 490mA(dots), 620mA(squares) and 760mA(triangles).

problem of the flux-modulated cores.

### 3.1.1 Residual modulation ripple in series feedback DCCTs

Since the development of the first wideband parametric beam DCCT consisting of a parametric current transformer (CT) and an active feedback CT (so-called L/R-integrator) by K. Unser in 1969 [16,17], the feedback circuit as shown in Fig. 23 has been widely employed for beam DCCTs where the feedback winding of the DC current detection core $L_3$, the feedback winding of the AC current detection core $L_3$, and the current sense resistor $R_f$ are connected in series. Hereafter, we call this configuration of the feedback circuit the "series feedback circuit". The flux modulation of the DC current detection cores induces a modulation ripple voltage $j\omega N_f \phi_r$ in the feedback coil $L_2$ due to a magnetic flux imbalance $\phi_r$ in the flux modulation between a pair of DC current detection cores $T_2$ and $T_3$. Although the ripple current induced in the feedback circuit is expected to be suppressed by the L/R-integrator, we have some residual ripple in the output signal because of a limitation of the open-loop gain due to the stability condition of the closed-loop response. Based on a linear circuit analysis, the feedback current $i_f$ is expressed by

$$N_f i_f = G(\omega) i_b + H(\omega) i_r, \tag{1}$$

and the output voltage is given by $v_{\text{out}} = R_f i_f$, where $i_b$ is the beam current, $i_r \equiv \left(N_f^2/L_3\right) \phi_r$ is the equivalent ripple current converted to the beam current appearing at the harmonic frequency $\omega = n\omega_m$ $(n = 1, 2 \cdots)$ of the parametric modulation frequency $\omega_m$, and $N_f$ is the number of turns of the feedback coils $L_2$ and $L_3$. The signal response function so called the closed-loop gain $G(\omega)$

and the ripple response function $H(\omega)$ are given by

$$G(\omega) = -\frac{G_0(\omega)}{1 + G_0(\omega)}, \tag{2}$$

$$H(\omega) = -\frac{j(\omega L_3/N_f R_f)g(\omega)}{1 + G_0(\omega)}, \tag{3}$$

where $G_0(\omega) = A_0(\omega) + K_0(\omega) + (j\omega L_3/R_f)g(\omega)$ is the open-loop gain function of the system, $A_0(\omega) \simeq A(\omega)N_f$ is the open-loop gain of the parametric-CT and $K_0(\omega) = (R_1 N_f/R_f N_1)f(\omega)\{K(\omega) + 1\}$ is the open-loop gain of the L/R-integrator. $K(\omega)$ is the gain function of the L/R-integrator amplifier, $A(\omega)R_f$ is the transimpedance of the demodulator of the beam current parametric modulation, $g(\omega) = 1/(1 + j\omega L_3/R - \omega^2 L_3 C)$ is the response function of a ripple-suppression filter consisting of $L_3$, $C$ and $R$, and $f(\omega) = (j\omega L_1/R_1)/(1 + j\omega L_1/R_1 - \omega^2 L_1 C_1)$ is the response function of the detection coil of the L/R-integrator, where $C_1$ is dominated by the signal cable capacitance.
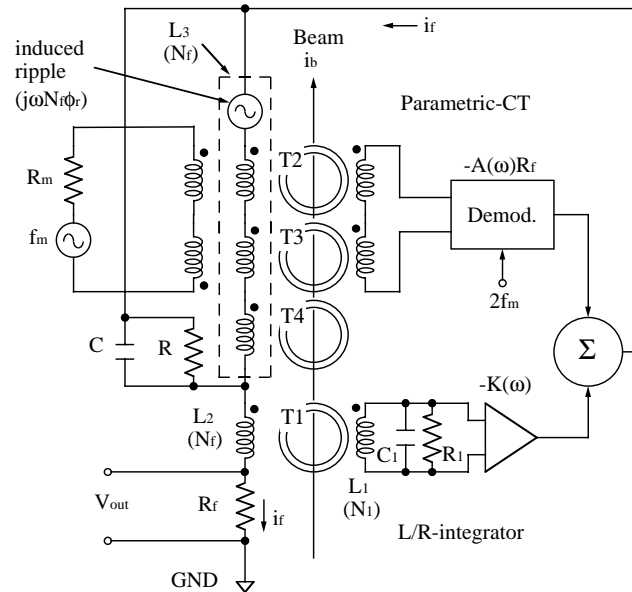


Fig. 23. Block diagram of the series feedback DCCT circuit.

Even though the low-pass filter in the demodulator of the parametric-CT is designed so as to suppress the ripple components in its output completely, some ripple component appears in the output signal $v_{out}$ by the coupling between the feedback coils $L_2$ and $L_3$ connected in series. If we have a 1% imbalance of the modulation flux in a pair of flux modulated cores, the equivalent ripple current $i_r$ would reach to the order of 10mA, and an extremely high open-loop gain of the L/R-integrator $K_0(\omega)$ is required from Eq. (3) to suppress the residual ripple in the output signal. However, the open-loop gain $K_0(\omega)$ is limited by the stability condition of the closed-loop gain $G(\omega)$. To suppress residual ripple caused by incompleteness of the ripple suppression due to the

limited open-loop gain, it is required not only to select a highly balanced pair of magnetic cores for parametric modulation [18], but also to design the ripple suppression filter $g(\omega)$ so as to satisfy the condition $|g(\omega)| \ll 1$ in the ripple frequency region, $\omega \geq \omega_m$. On the contrary, it is required that $g(\omega)$ should not be so small because the open-loop gain $A_0(\omega)$ of the parametric-CT is proportional to $g(2\omega_m)$, where $2\omega_m$ is the demodulation frequency of the demodulator. These incompatible requirements make the design of $g(\omega)$ difficult, and we need a complicated empirical determination of the circuit parameters because of ambiguities in the effective inductance $L_3$ due to the flux modulation exceeding saturation in the flux-modulated cores and in the effective resistance $R$ dominated by core loss. Indeed, we could not suppress the residual modulation ripple to a sufficiently small level for the beam-current measurement with non-selected magnetic core pairs by optimizing $g(\omega)$.
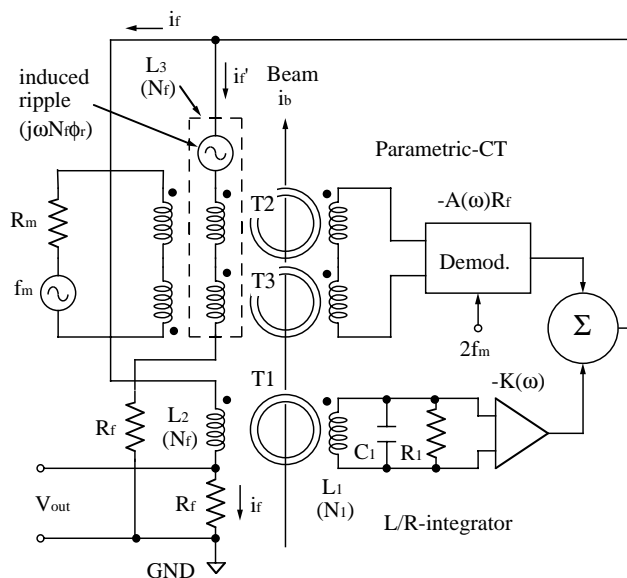


Fig. 24. Block diagram of the parallel feedback DCCT circuit.

### 3.1.2 Parallel-feedback DCCTs

To avoid any complicated ripple-suppression problems, we developed the "parallel feedback circuit" shown in Fig. 24 [6], where the feedback coils $L_2$ and $L_3$ of the parametric-CT and of the L/R-integrator are connected in parallel and the output signal is taken from the current sense resistor connected in series to $L_2$. By employing the parallel-feedback circuit, we have obtained a null response for the ripple noise, *i.e.* $H(\omega) = 0$, if the low-pass filter in the demodulator of the parametric-CT is designed to suppress the ripple noise completely in its output, since the neither the transformer of the L/R-integrator nor the current sense resistor pick up the induced ripple current in $L_3$. As for the signal response function $G(\omega)$, a linear-circuit analysis guarantees the same closed-loop gain as that of the series feedback DCCT, since the closed-
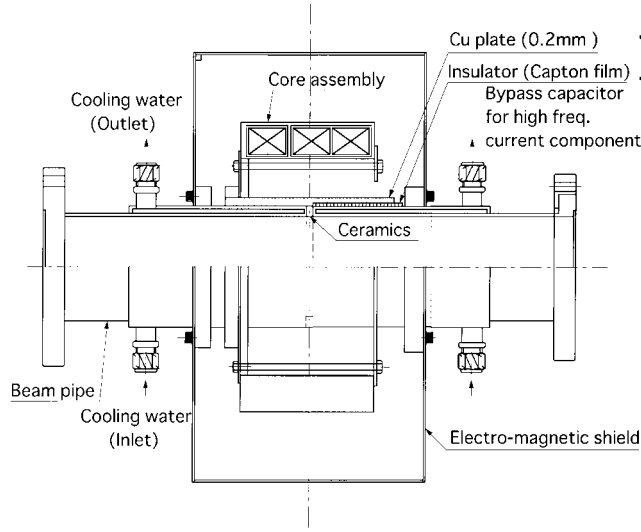
Fig. 25. The schematic drawing of the DCCT core housing.



Fig. 26. A DCCT (front side) and a CT (back side) installed in the LER.

loop signal gain function $G(\omega)$ is given by Eq. (2) with the open-loop gain of $G_0(\omega) = A_0(\omega) + K_0(\omega)$, which is the same as the open loop gain of the series feedback DCCT, except for the coupling term, $j\omega L_3/R_f$, caused by the series connection of feedback coils $L_2$ and $L_3$. The output of the DCCT with the parallel feedback circuit is essentially free from ripple noise. We do not need not only a special ripple-suppression filter, such as $g(\omega)$, but also ripple suppression by the open-loop gain of the L/R-integrator, even if a magnetic-flux imbalance exists in a pair of cores for parametric modulation. Therefore, the parallel feedback circuit for the parametric DCCT makes it possible to use non-selected magnetic core pairs without any complicated ripple-suppression technique.

Based on the above arguments, we developed new DCCTs with parallel feed-back circuits for the KEKB electron and positron storage rings to overcome core selection problems. For DC current detection by parametric modulation, a pair of magnetic cores of strip-wound toroids (25mm thich tape of Ni-Fe-Mo alloy, TMC-V/TOKIN) are employed without pairing. The magnetic cores are assembled inside a magnetically shielded case, and installed in the core housing mounted on the accelerator, as shown in Figs. 25-26. To avoid coupling between the transformers of the parametric-CT and of the L/R-integrator, each transformer is separately shielded by high-$\mu$ metal, since the field leak-age from the flux modulated cores to the L/R-integrator core causes a residual modulation ripple in the output signal. A ceramic break in the beampipe in-side the core housing is straddled by a cylindrical capacitor ($\approx$100pF ) made from double layers of a thin Cu plate and a Capton film in order to bypass the high-frequency component of the beam-induced current on the beampipe. The DCCT head is connected by a 100 meter-long signal cable to an elec-tronic circuit installed in a local control building. The parametric modulation frequency is designed to be 1 kHz and the demodulation frequency is 2 kHz.
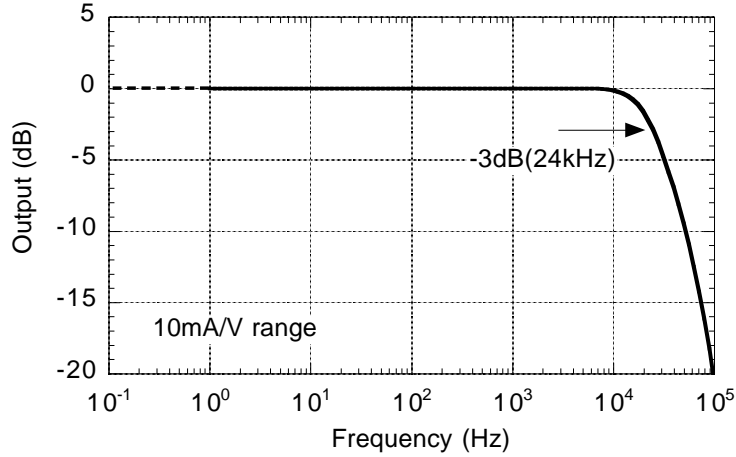


Fig. 27. Frequency response of the parallel feedback DCCT.

Figure 27 shows the frequency response, where the cut-off frequency 24kHz is limited by the signal cable capacitance of $C_1 = 18$nF and the input impedance of the L/R-integrator of $R_1 = 220\Omega$. In spite of the wideband response, we succeeded to suppress the residual ripple noise to an order of $\mu$A, as shown in Fig. 28 and in Table 3, without selected pairing of the magnetic cores for the parametric flux modulation.

Table 3
Residual ripple components converted to the equivalent beam current in the output of the parallel feedback DCCT.

| Frequency (kHz) | 1 | 2 | 3 | 4 | 5 |
|---|---|---|---|---|---|
| Residual ripple ($\mu$A$_{\text{rms}}$) | 0.50 | 0.35 | 1.27 | 0.19 | 0.54 |

Every one second, one of the IOCs of the KEKB EPICS system samples the

Fig. 28. Output noise of the parallel feedback DCCT developed for the KEK B-factory. The vertical scale is $20\mu$A/div and the horizontal scale is 0.2ms/div.

beam current measured by the DCCT. Additionally, an analog signal whose level is propotional to the measured beam current is disributed to several control stations along the rings. Figure 29 is an example of the beam-current record during one day displayed on the accelerator operation console.



Fig. 29. An example of the beam-current record of the HER and LER during one day.

*3.2 CTs*

Besides a DCCT, we have a simple CT with a ferrite toroid wounded by a copper wire of 10 turns in each ring (Fig. 26). This type of CT is available to observe beam bunches only during single-bunch operation because of a poor time response on the order of nsec. However, the CT signal is useful to search the beam-storage condition in the beam injection tuning to the ring. In Fig. 30, the first beam in the HER observed by the CT at the first commissioning in

25

December, 1998, is shown, where an electron bunch with about 0.2nC turned around in the ring.
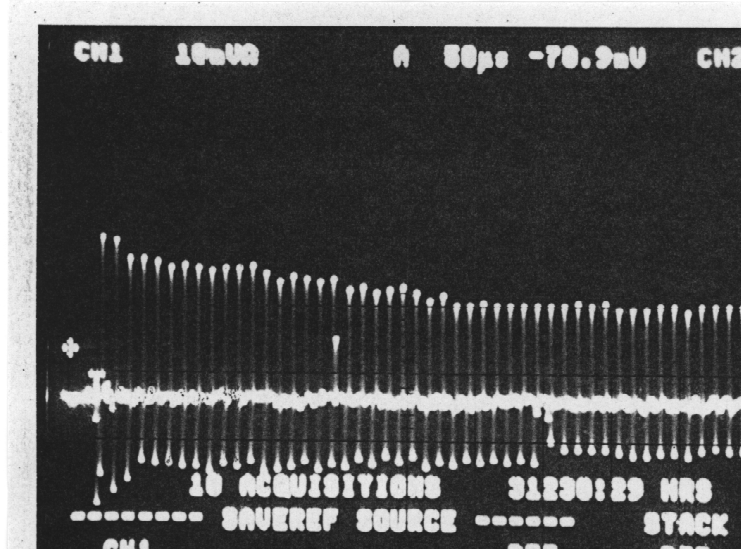


Fig. 30. The first beam turning around in the HER observed by a CT.

## 4 Bunch feedback systems and related systems

At the design stage of KEKB, we expected very strong coupled-bunch instabilities, particularly in the transverse planes. In order to suppress them, we desinged and constructed very wide-band bunch-by-bunch feedback systems for both the transverse and longitudinal planes. Through the operation experiences of KEKB, we have found that the transverse instabilities are actually so strong that feedback systems are indispensable for the operation of the rings. On the contrary, we have not encoutered any serious longitudinal instability, and therefore, we heve not operated the longitudinal system up to July, 2001.

### 4.1 Transverse bunch feedback systems

The structure of the transverse feedback system is schematically explained by the block diagram showin in Fig. 31. Each component is installed in the Fuji corossing area as, shown in Fig. 32. There are two BPM sections in each ring to make a suitable betatron phase-rotation from the monitor to the kicker by vectorially combining the two signals from the upstream and downstream beam position pickups. The phase advance and the betatron function at the BPMs and the kickers are listted in Table 4. The major part of closed orbit distortion (COD) at the BPMs is suppressed by continuous closed-orbit
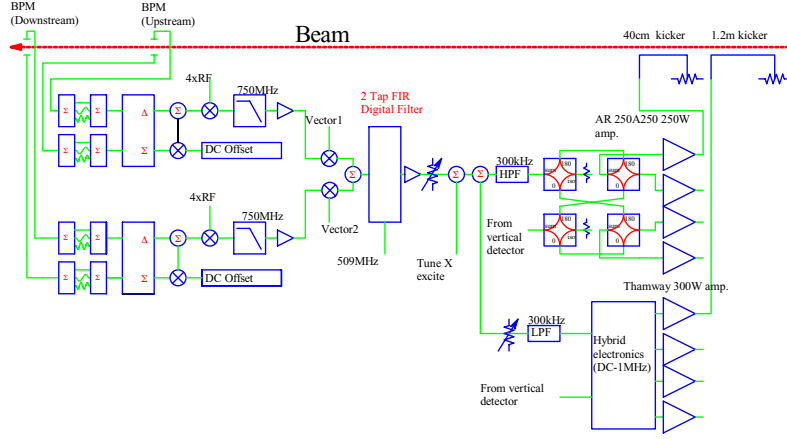
26

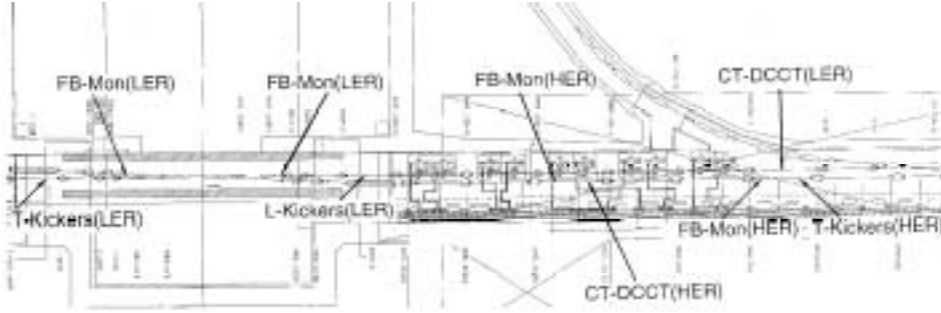Fig. 31. Block diagram of the transverse feedback systems.



Fig. 32. Location of the feedback equipment at the Fuji crossing area. Positrons come from left side and electrons come from the right side. All the final feedback amplifiers are installed under the crossing bridge.

correction (CCC). Residual CODs are cancelled by the local offset canceller circuit.

The signal processing is performed with a specially designed board whose main function is a two-tap digital filter (the digital filter board). The design and peformance of the board is closely described in Reference [4]. Figures 33 and 34 show a photo and a block diagram of the digital filter. The functions of the two-tap FIR filter are: (1) rejection of any DC component including an error in the detection circuit, (2) pick up the betatron-tune component, and (3) digital delay to adjust the one-turn delay. The tap positions of the filters are set with (kick) $\propto$ (position data 2 turns before ) $-$ (position data 1 turn before) because the fractional part of the betatron tunes are around 0.5. The residual phase errors coming from the phase shift in the filter function are corrected with fine tuning of the vectorial combiner.

Stripline-type kickers for transverse deflection are installed upstream of the first position pickup. We use two kinds of transverse kickers, a 40 cm wideband kicker up to 255MHz and a 1.2 m lower frequency kicker for frequencies below 1 MHz. Four 250W amplifiers (10 kHz–250 MHz) to drive the 40 cm kicker and

Table 4
Feedback-related parameters of KEKB.

| Ring | LER | HER | |
|---|---|---|---|
| Energy | 3.5 | 8.0 | GeV |
| Circumference | 3016.26 | | m |
| Bunch current | 0.76 | 0.67 | mA |
| Betatron tune | 45.53 /43.58 | 44.5 2 / 41.62 | |
| rf voltage | 6.0 | 11.0 | MV |
| rf Frequency | 508.887 | MHz | |
| Damping time (L) | 22/23 | ms | |
| Betatron functions | $\beta_x/\beta_y$ | | |
| BPM1 | 21m/21m | 19m/16m | |
| BPM2 | 21m/21m | 30m/8m | |
| Kickers | 23m/7m | 33m/14m | |
| Phase advance | $\Delta\nu_x/\Delta\nu_y$ | | |
| BPM1 - BPM2 | 65°/65° | 88°/107° | |
| Kicker - BPM1 | 18°/48° | 10°/12° | |



Fig. 33. Photo of the digital filter board.

four 300W amplifiers (5 kHz–1 MHz) to drive the 1.2m kicker are used for each ring. Since the performance of the wideband amplifiers below 50 kHz is not ideal, and an intentional injection error (kicker jump) has only low frequency components, we use the lower-frequency system to help the damping around the lowest mode of the beam oscillation. To equalize the two bands, we use 1st order low-pass and high-pass filters with a crossover frequency of 300kHz.
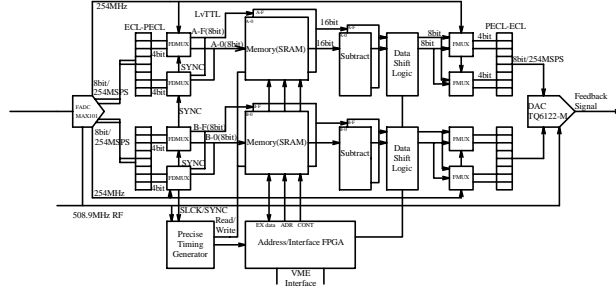
Fig. 34. Block diagram of the filter board.

### 4.1.1 Progress of the operation of the feedback systems

During the early stage of commissioning the feedback systems [5], we used only the wideband kicker systems so as to avoid any complexity comming from equalization of the overlapping bands. The digital filter worked as a simple digital delay, not as a two-tap filter. Under this condition, we experienced several difficulties:

- Unexpected power saturation at the final power amplifiers. Since the residual offset of a detector depends on both the bunch current and beam phase shift due to beam loading, it is impossible to cancel out the offset with the analog circuit. The saturation reduced the dynamic range of the feedback system and restricted the gain of the system to be lower than the expected one.
- Insufficient damping rate at injections. The amplifiers always saturate at the injection period due to a large injection bump error. The system worked as a bang-bang damping scheme during injection, and the performance was greatly reduced.

By changing the function of the digital filter from the simple delay mode to the two-tap FIR mode, the position offsets between the bunches have been completely cancelled out. This offset compensation has enabled us to increase the feedback gain without saturation at the amplifiers. The huge perturbation during injection is now suppressed well by adding the lower frequency system and equalizing the wideband system.

### 4.1.2 Performace of the transverse feedback systems

We have esitimated the performance of the feedback system by actuallly measuring the damping rate of the horizontal oscillation during injection using a bunch oscillation recorder [4]. Figure 35 shows an example of damping of the horizontal oscillation during injection of the HER with a total current of around 730 mA. The present setting of the feedback damping times at the maximum beam current are 0.2 ms (horizontal:H) and 0.8 ms (vertical:V) in the HER, and 0.2 ms (H) and 0.4 ms (V) in the LER, respectively.
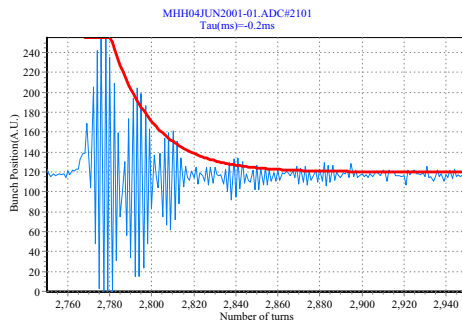
29

Fig. 35. Feedback damping of injection oscillation (horizontal) in the HER at current of 730 mA.

During normal operation for physics runs, we fill the beam in every 4th rf-bucket (8 ns spacing) with a gap space for the beam abort kicker, with a total bunch number of 1155 per ring. Under this fill pattern, the growth times of the instabilities in the LER are less than 0.5 ms in the horizontal plane, and a few ms in the vertical plane. In the HER, the growth time is about a few ms for both the horizontal and vertical planes. The feedback system has shown much better performance than the design.

## 4.2  Beam diagnostic systems based on the feedback electronics

The digital filter board for the bunch-by-bunch feedback systems was designed to handle beam bunches with a frequency of 509 MHz; the front part of the circuit can be used as a powerful tool for beam diagnostics. We modified the signal-process board by removing the output part and adding memory chips to store various bunch-by-bunch/turn-by-turn information of bunches. This board is called the *memory-board*.

### 4.2.1  Bunch current monitors

We prepared a special detector-circuit which can detect the intensity of individual bunches in the ring. The memory-board accepts the output of the detector, i.e., the ADC on the board converts the detector-output into a digital signal, and the converted data is recorded in memory chips on the board. The stored data is read out from the memory and converted to the bunch-current by multiplying a factor which is calibrated by the DCCT signal. Figure 36 shows two examples of the bunch-current information displayed on the operators' console.

Fig. 36. Two examples of the bunch-current monitor output. Special filling pattern before (upper) and after (lower) switching off/on the feedback are shown.

### 4.2.2 Bunch oscillation recorder

A second example of applications of the memory-board is recording oscillations (mainly transverse) of bunches in a ring. We call the memory board tuned for this purpose a *bunch oscillation recorder* (BOR). Figure 37 shows the growth of oscillation of a bunch (bunch ID = 4800) in the LER recorded by a BOR. By analyzing the data, we have found that the growth time is shorter than
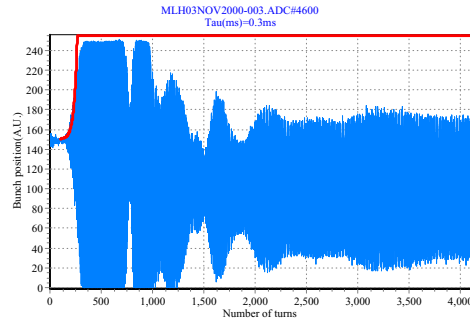


Fig. 37. Recorded growth of the instability using the bunch oscillation recorder. The growth time was about 0.3 ms. The beam was lost within several hundred turns.

0.5 ms, and that the mode distribution around the lowest modes is rather broad, as shown in Fig. 38.

In order to investigate the cause of a sudden beam loss during operation, we are now testing beam-loss trigger systems to record the beam behavior just
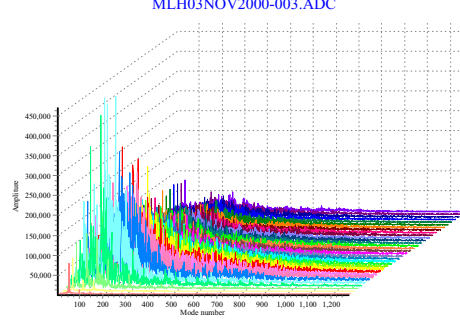
31

Fig. 38. Result of the mode analysis of the growth observed in the LER. The modes are concentrated around the lower mode, but the distribution is not so narrow.

before the beam loss with the BORs. An example of the growth of vertical oscillation and its mode analysis just before beam loss in the HER are shown in Figs. 39 and 40, respectively.
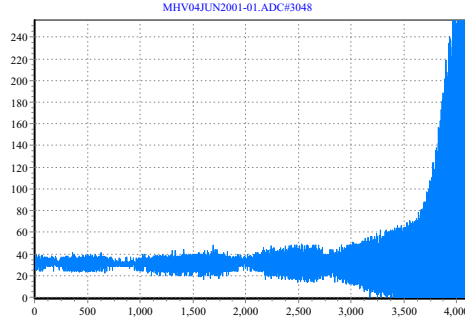


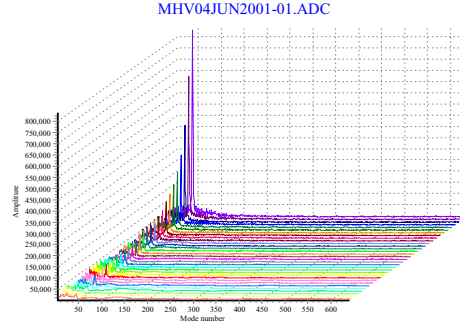Fig. 39. Growth of vertical oscillation just before beam loss in the HER.



Fig. 40. Result of the mode analysis of the growth. The growing mode is around mode 41 and is very narrow, like single mode.

## 5   Tune measurement sytems

A continuous tune measurement is highly required for the stable operation of KEKB. Since KEKB is operated at the horizontal betatron tune close to

a half integer, the beam lifetime and the modulation of the optical function by a beam-beam force are sensitively affected by the tune. However, in beam colliding operation we encounter a difficulty for precise tune measurement, because the beam-beam force modulates the tune and several peaks appear in the tune spectrum. In order to avoid this difficulty, a non-colliding bunch (so-called a "pilot bunch") is intentionally stored in the abort gap, and the tune of the pilot bunch is continuously monitored.

The tune meter system [20] is combined in the bunch-by-bunch feedback system, as shown in Fig. 41. The bunch signal from the button electrode mounted on the beampipe is gated to select the pilot bunch signal, and its oscillation is detected by a sweeping frequency method using a tracking analyzer (Anritsu, MS420K). The output of the tracking analyzer is swept in frequency corresponding to a fractional part of the betatron tune (1–50 kHz), and modulates a pulse of 50 ns-width synchronized with the revolution frequency of 99.39 kHz to form a "deflection pulse", which is combined with the bunch-by-bunch feedback signal for the feedback-kicker to excite the betatron oscillation of the pilot bunch. The resolution of a tune measurement is mainly determined by the bandwidth of the tracking analyzer, and is estimated to be ±0.0004 in the present configuration. Examples of the tune spectra measured during the colliding-mode operation of the KEKB rings are shown in Fig. 42. We observe significant broadening in the horizontal tune spectrum of the LER, and it is caused by damping action of the bunch-by-bunch feedback and by overlapping of the spectrum cuased by aliesing around a half-integer tune.
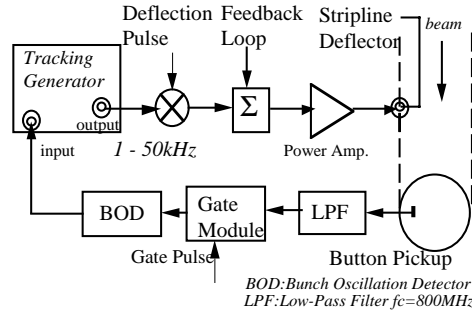


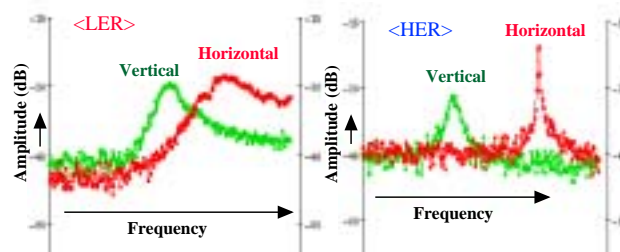Fig. 41. Scheme of the gated tune measurement system.



Fig. 42. Examples of the tune spectra, left: for the LER, total width of the horizontal axis corresponds to the tune of 0.06. Right: for the HER, total width of the horizontal axis corresponds to the tune of 0.07.

In addition to the tune measurement for tune manipulation of the rings during physics runs, the gated tune meter enables us to investigate the tune variation of an individual bunch along the bunch train. In the LER, it is expected that the betatron tune of the positron bunch is increased by focusing action of the photo-electron cloud. By sweeping the gate timing of the bunch-selection gate and of the deflection pulse synchronously, the horizontal and the vertical tune shifts of an individual bunch in the bunch train are measured, as shown in Fig. 43, where the variation of vertical tune shift along the bunch train caused by the accumulation of photo-electron clouds is clearly observed. In the bunch-gap region, even though the electron clouds decrease rapidly, a significant amount of the electron density remains even after 100 empty rf-buckets. These results provide important information on the photo-electron density in the vicinity of the positron beam. In this measurement, the oscillation amplitude excited by a deflection pulse was restricted to within the vertical beam size, so as not to disturb the electron cloud. We also carefully checked the effect of the preceding bunches in the rising edge of the deflection pulse, and confirmed no meaningful effect on the measurement.
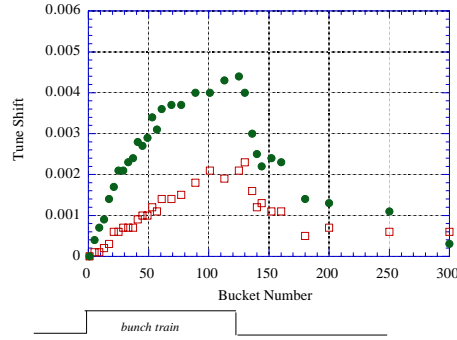


Fig. 43. Tune shift along a train and that after a train vs. bunch number measured with the solenoids turned on. The train contains 32 bunches with a 4-bucket spacing. Squares are the horizontal tune shift and dots are the veritcal one. The tune after the train was measured for each bunch placed to observe.

## 6 Optical diagnostic system

Measuring the beam profile or beam size using the synchrotron radiation improved the efficiency of the commissioning of KEKB. A beam-monitor system by means of synchrotron radiation (SR) for KEKB was designed and constructed. A visible SR beam for the monitor is produced by a dedicated weak bending magnet, and is extracted by a mirror system which undergoes a real-time mirror-surface flatness measurement. The extracted SR beam is transferred to the SR monitor hat on the ground by an about 40 m long optical-path system. An image of the electron (positron) beam is observed by

using a focusing system. The SR interferometer is applied to measure both the horizontal and vertical beam sizes. Extra few branch beam lines are prepared for the other measurements, such as streak camera and fast gated camera. The beam images for the HER and the LER are continuously displayed in the control room and an automatic analysis system for an interferogram via the SR interferometer runs on the control computer [21].

## 6.1 SR source and extraction system

We inserted dedicated 5 mrad weak bending magnets into both the HER and the LER as SR beam sources to reduce the strong power of the SR beam due to hard X-ray component. The bending radii are 65 m for the LER and 650 m for the HER, respectively. The total angular radiation powers of the SR beams are 55.9 W/mrad for a 2 A beam in the LER and 76.3 W/mrad for a 1A beam in the HER. The SR beams from the weak beading magnets are extracted by a water-cooled beryllium extraction-mirror. The surface temperature was estimated to be 60°C for the maximum power input by a thermal simulation. To watch the thermal deformation of a beryllium extraction-mirror, we set a Shack-Hartmann wavefront sensor [22]. An outline of the extraction-mirror system is shown in Fig. 44. The mirror chamber has a double structure, i.e. an inner duct and a surrounding chamber. The inner duct is designed to maintain electrical smoothness of the duct surface so as to reduce the corrective effects. A water-cooled beryllium mirror is inserted inside the duct. The duct has a surrounding chamber to maintain an inside vacuum, and the chamber has two holes that face the beryllium-mirror. One is for the extraction of a visible SR beam; other is to watch for any thermal deformation of the mirror surface, as shown in Fig. 44. These holes on the inner duct are covered with 5mm thick optical-quality quartz plates. Since the inside of the quartz plate faces an electron or positron beam, we applied a 500 nm thick Ti coating. This coating effects only a neutral-density filter in the optical design of the system.
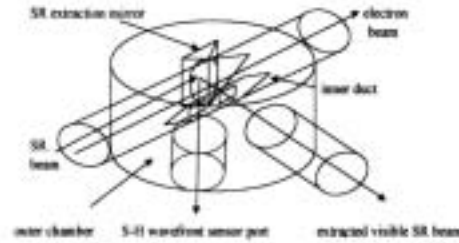


Fig. 44. A schemativ view of the SR extraction mirror system.

The temperature of the chamber rises from 25°C to 47°C due to a ring current of 500 mA. This temperature rise is proportional to the ring current. Since we did not observe any non-linear temperature rise, the design of the chamber is well functioned to prevent corrective effects. An electric fan is applied to cool the chamber.

## 6.2 Optical path to monitor hut

After the extraction mirror, the SR beam is divided into two beams for two branch beamlines by a beam splitter (2 : 98). Since the focusing system does not require an intense beam, we supply 2% of the total beam for the focusing system (beamline No.1). The remaining 98% is supplied for the SR interferometer and other instruments used for machine studies (beamline No.2). The beamline for the focussing system has a relay lens system to reduce the conjugation ratio of the focussing system. The total length of the optical path is about 40 m and is closed by aluminium tubes and boxes (not evacuated). Each beamline is aligned by the auto-collimation method using a He-Ne laser. An outline of the optical path is shown in Fig. 45 [23].

At the end of the optical path, two SR monitor huts are set on the ground floor. One is dedicated for an SR interferometer to monitor the vertical and horizontal beam sizes. The other hut has a focusing system and equipment for machine studies.

## 6.3 Imaging system for profile measurements

A conventional beam-profile monitor based on a focusing system is set at the end of beamline No.1. Figure 46 shows a typical example of the beam profiles for the HER and the LER. The focussing system consists of a relay lens system (set in the beamline), a diffraction-limited doublet lens (F=1000mm) for the objective, a magnifier lens and a CCD camera. The conjugation ratio of the objective including the relay lens is 0.025.

## 6.4 SR interferometer for monitoring the beam size

To monitor the beam size, SR interferometers [24] are applied to both the HER and LER. Two branch beamlines are cut from beamline No.2 by a totally reflecting mirror. Two independent SR interferometers are set at the end of these branch beamlines for measurements of both vertical and horizontal beam
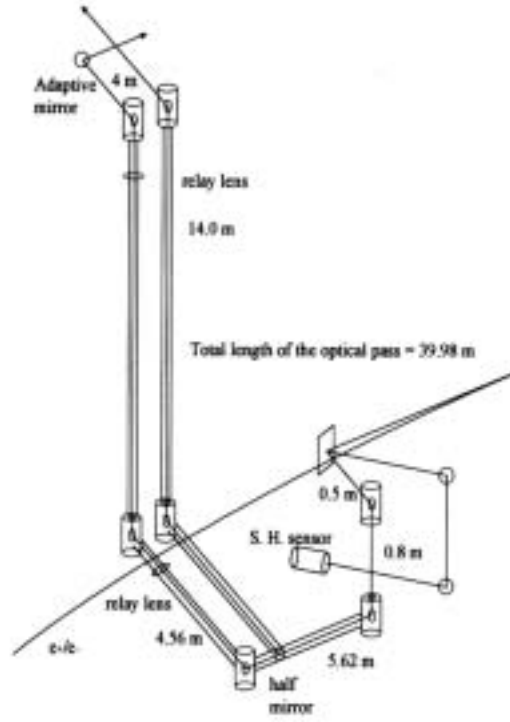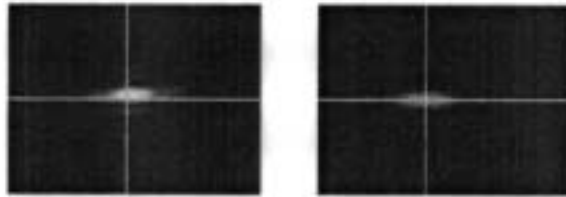
Fig. 45. Outline of optical path.



Fig. 46. Observed beam profiles.

sizes. The arrangement of the SR interferometer is shown in Fig. 47. We use a fixed slit separation for beam-size monitoring.
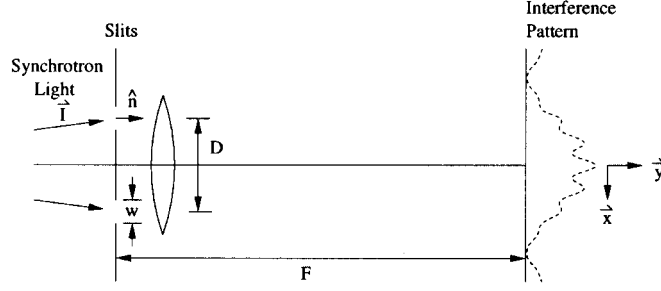
Fig. 47. A set up of the SR-interferometer.

*6.5   Automatic beam-size measurement system*

Using a Gaussan beam-profile approximation again, we can estimate the RMS beam size from one data concerning visibility of one interferogram, which is measured at a fixed separation of two slits (the double slit) [24]. For a single-wavelength $\lambda$ of the incident SR, the interferogram from the double slits having a separation of $w$ has an intensity distribution $y(x)$ of the form [22]:

$$y(x) = I_0 \left[ \frac{\sin(\frac{2\pi}{\lambda}\frac{w}{F}x)}{\frac{2\pi}{\lambda}\frac{w}{F}x} \right]^2 \left( 1 + \gamma \cos\left( \frac{2\pi D}{\lambda F}x \right) \right),$$

where $I_0$ is the intensity of the light reaching each slit, assuming the intensities $I_1$ and $I_2$ at each slit are equal ($I_1 = I_2 \equiv I_0$). This represents two single-slit diffraction patterns $(\sin(x)/x)^2$ brought into overlap by a lens behind the slits, modulated by a cosine double-slit term with visibility $\gamma$ determined by the spatial coherence of the SR light. The CCD imaging plane is at a distance $F$ from the secondary principal point of the lens. The visibility is the desired quantity, from which the beam size is calculated, assuming a Gaussian beam distribution. The RMS beam size $\sigma_{\text{beam}}$ is given by

$$\sigma_{\text{beam}} = \frac{\lambda R}{\pi D} \sqrt{\frac{1}{2} \ln\left( \frac{1}{\gamma} \right)},$$

where $\gamma$ denotes the visibility, which is measured at a double-slit separation of $D$; $R$ is distance between the beam source point and the double slit [24]. We can easily measure a beam size automatically from an analysis of the interferogram taken at fixed separation of the double slit, $D$ [21]. To find the visibility $\gamma$ from the interferogram, we use the standard Levenberg-Marquart method for non-linear fitting [26]. Due to mirror distortions arising from heating of the extraction mirror, changes in the apparent beam size due to the mirror-surface curvature and light imbalances between the two interferometer slits need to be taken into account. Accordingly, we need to modify the above simplified equation and so fit the interference pattern to an equation of the form

38

$$y(x) = a + bx$$
$$+ \frac{m}{2} \sum_i t_i \left\{ A_1^2 + A_2^2 + 2A_1 A_2 \gamma^{\left(\frac{\lambda_0}{\lambda_i}\right)^2} \cos\left[\beta_c \left(\frac{\lambda_0}{\lambda_i}\right)(x - \phi_c)\right] \right\},$$

where

$$A_1 = \sqrt{1 + \alpha_I} \frac{\sin\left[\beta_s \left(1 + \alpha_s\right) \left(\frac{\lambda_0}{\lambda_i}\right)\left(x - \left(\phi_s - \frac{\delta_s}{2}\right)\right)\right]}{\beta_s \left(1 + \alpha_s\right)\left(\frac{\lambda_0}{\lambda_i}\right)\left(x - \left(\phi_s - \frac{\delta_s}{2}\right)\right)},$$

$$A_2 = \sqrt{1 - \alpha_I} \frac{\sin\left[\beta_s \left(1 - \alpha_s\right) \left(\frac{\lambda_0}{\lambda_i}\right)\left(x - \left(\phi_s + \frac{\delta_s}{2}\right)\right)\right]}{\beta_s \left(1 - \alpha_s\right)\left(\frac{\lambda_0}{\lambda_i}\right)\left(x - \left(\phi_s + \frac{\delta_s}{2}\right)\right)}.$$

The two single-slit diffraction terms are represented by amplitudes $A_1$ and $A_2$. The cos term has a period determined by $\beta_c$, with an offset of $\phi_c$. The resulting pattern is of magnitude $m$, with a linear background term, $a + bx$.

To account for bandpass effects, which would otherwise artificially lower the visibility, we write the fitting function as a sum over a sample of wavelengths $\lambda_i$ passed by the bandpass filter with central frequency $\lambda_0$, with each term being weighted by the transmission $t_i$ at that wavelength. The incident SR spectrum changes by only a few percent over the bandwidth used (10 nm, centered around 500 nm), and is taken as flat. The exponent appearing on $\gamma$ represents the variation of visibility observed at different wavelengths relative to that observed at the central wavelength, assuming a Gaussian beam with the same apparent beam size at all wavelengths (i.e., using the previous equation).

Regarding the $A_1$ and $A_2$ terms, $\alpha_I$ represents the asymmetry $\frac{I_1 - I_2}{I_1 + I_2}$ of the light intensities $I_1$ and $I_2$ impinging on the two slits. $\beta_s \left(1 \pm \alpha_s\right)$ represent the widths of the single-slit $sinc$ terms from each slit, with $\alpha_s$ representing the (usually very small) asymmetry between the widths of the patterns from each slit. $\phi_s \pm \frac{\delta_s}{2}$ represent the centers of the single-slit terms, separated by $\delta_s$ from each other. Changes in $\delta_s$ are correlated with the deformations in the mirror. The deformation can be measured by use of the Hartmann mask (see next section), but the interferometer cannot be used at the same time as the Hartmann mask. By measuring $\delta_s$ the deformation can be monitored and corrected for in real-time during interferometer usage. This compensation mothod makes us free from mirror deformaiton problems.

The fit results are sent to an EPICS IOC host, which calculates the beam size at the SR-source bend, and maps the result to the interaction point via the beta functions. After the image processing of the interferogram, the results are displayed on a CRT panel in the control room. Fig. 47 shows an example of the display panel for the LER. A same panel is also displayed for the HER.

The interferogram, best-fit curve and beam-size trend graphs for the vertical and horizontal directions are shown in the panel. By this automatic beam-size measurement system, we can measure the vertical and horizontal beam sizes every 0.2 seconds, and which are extremely useful for beam-tuning.
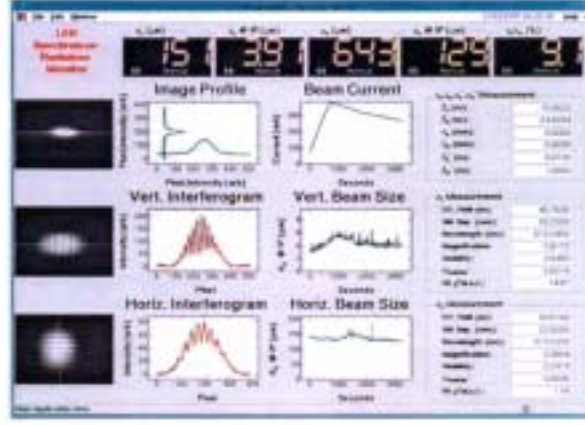


Fig. 48. SR Monitor panel in the control room, showing the LER vertical and horizontal beam sizes.

*6.6  Deformation of the SR extraction mirror*

The extraction mirror for the SR beam is deformed by strong irradiation of SR. The actual rays due to this deformation propagate over different optical paths compared with ideal rays. Therefore, the two optical paths of actual rays those arriving at the double slit give a different separation from that of the ideal rays. We must know the true separation of the two rays at the location of the double slit. To measure the wavefront error and true separation of two rays, we applied the Hartmann screen test. In this test, the wavefront is sampled by a number of rays normal to it, and the ray deviation at the observation plane can be obtained. We used a 100-hole square-array screen as shown in Fig. 49. The interval of holes is 5mm. The square-array screen is fixed on an X-Y moving stage.

The setup for a wavefront-error measurement at the Photon Factory is shown in Fig. 51. With this setup, if we measure the dot positions of the Hartmann pattern on the observation plane with 0.1mm resolution, we can measure the wavefront with $\lambda/6$ (here, $\lambda$ is 633nm) precision.

To determine the true separation between the two rays at the location of the double slit, we use a single-hole screen, as shown in Fig. 51. The paths of two ideal rays are probed by scanning the single-hole screen in the plane perpendicular to the optical axis.
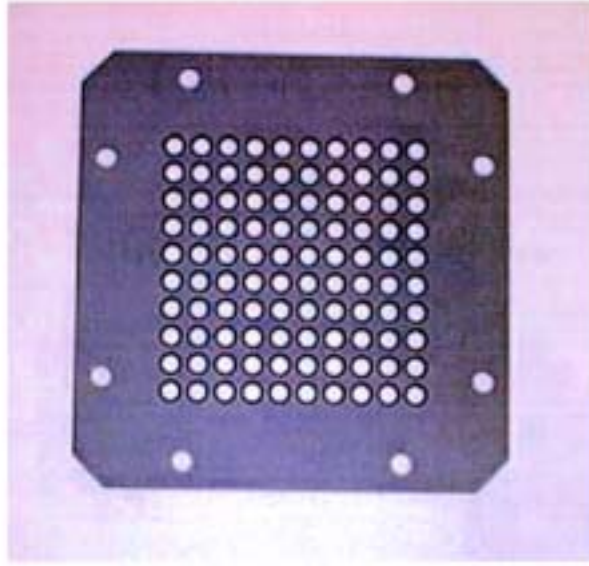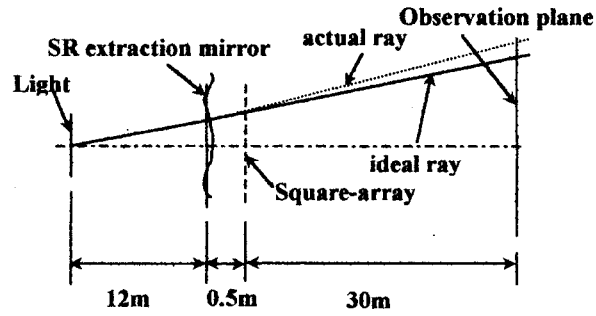
Fig. 49. A 100-hole square-array screen.



Fig. 50. Measurement set up.

*6.7 Optical-axis stabilization*

As the beam intensity changes and the mirror heats up, not only the mirror surface becomes deformed, but due to the way the mirror is mounted the orientation of the mirror also changes. This change in the mirror angle causes the angle of the optical axis to shift by unacceptable amounts once the light has propagated 30 m downstream to the optical hutch. To correct for this shift, we monitor the central position of the interference patterns on the camera face, and adjust the orientation of the mirror which is just downstream (35 cm) of the extraction mirror. This optical-axis feedback operates on a 10-second cycle. Typical feedback-compensation angles (the inverse of the mirror angle)
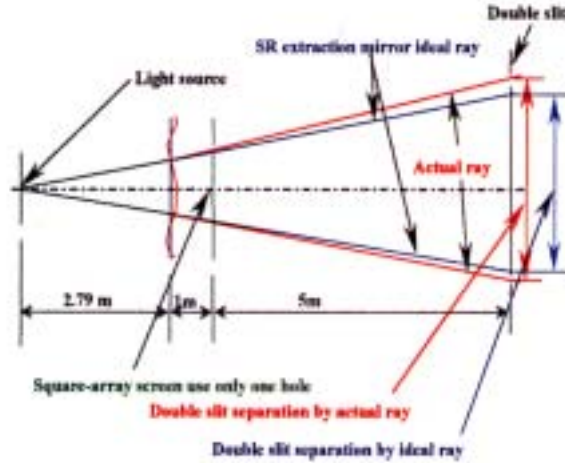
Fig. 51. Setup of determination of true double slit separation by scanning a single-hole screen.

are shown in Fig. 52 for the LER mirror over the course of several fills from a cold start. The vertical angle changes over a span of 1 mrad for the vertical axis, and about 0.5 mrad for the horizontal axis, with significant hysteresis. Optical-axis feedback is employed for both the LER and the HER mirrors.
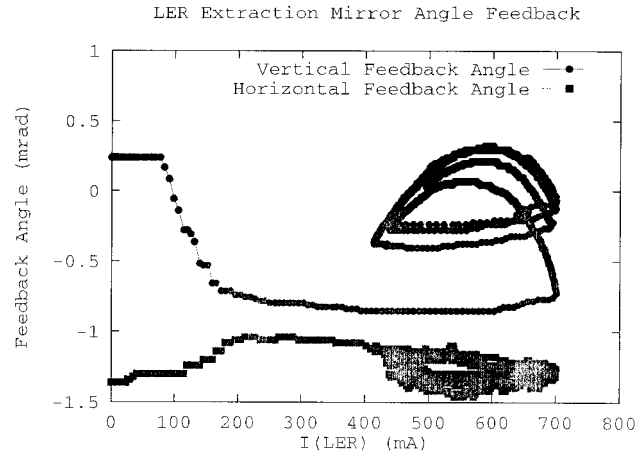


Fig. 52. Mirror feedback history from cold start through several fills.

## 6.8  Equipment for machine studies

Some equipment is set at the end of Branch beamline No.2 for machine studies. Here, we introduce bunch-length measurements using a streak camera and instantaneous beam-profile measurements using a high-speed gated camera.

### 6.8.1 Bunch-length measurements with a streak camera

The bunch lengths in the HER and the LER are measured by using the streak camera. The results of the bunch lengths as a function of the ring current are shown in Fig. 53.
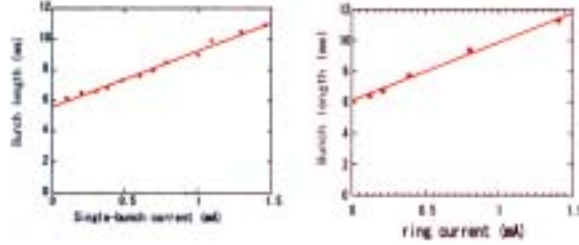


Fig. 53. Results of bunch length measurements.

We can estimate the natural bunch length by extrapolating the data to zero current; the results are 5.5 mm for the HER and 6.0 mm for the LER.

### 6.8.2 Beam-profile measurements with a high-speed gated camera

To observe instantaneous beam profile for bunch by bunch, we applied high-speed gated camera (Hamamatsu) [25]. With this camera, we observed blow-up of the bunch by bunch vertical beam-size along the bunch train in the LER. A typical result is shown in Fig. 54.
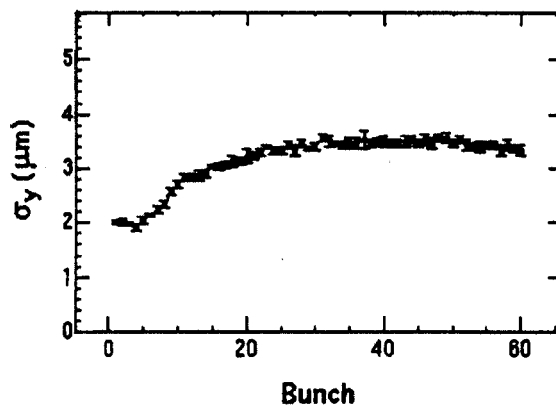


Fig. 54. Blow up of the bunch by bunch vertical beam-size along the bunch train in the LER.

## 7 Bunch-length monitors

Although streak cameras are widely used to observe the longitudinal bunch profile, an electronic measurement based on the bunch-spectrum analysis is considered to be another excellent way to measure the bunch length because of ease and quickness of the measuring process. Two types of monitors dedicated to the bunch-length measurement have been developed for KEKB. One is an RMS bunch-length monitor which evaluates the bunch length by detecting the two frequency components of the bunch spectrum. Another is a vacuum-free wideband pickup installed in the wavegide for the rf cavity where the bunch spectrum in the frequency region of 5–20 GHz is observed to caltulate the bunch length.

### 7.1 RMS bunch-length monitor

### 7.1.1 System

Suppose that $f(t)$ is a distribution function of a bunch. Its frequency spectrum is defined by the Fourier transform, $F(\omega) = \int_{-\infty}^{+\infty} f(t)e^{-j\omega t}dt$. Since $f(t)$ forms a bunch, one can limit the integral time region and may set $\omega t < 1$ by a proper choice of the frequency. The exponential term can be expanded in a series and the amplitude of the spectrum with an approximation to the second-term is given by [7]

$$|F(\omega)| \approx I_0 \left( 1 - \frac{1}{2} \left\langle t^2 \right\rangle \omega^2 \right).$$

(4)

Here, $\langle t^2 \rangle$ is the variance in the bunch distribution. The amplitude of the spectrum drops as $\omega^2$. In order to investigate the frequency dependence, a Gaussian bunch was compared with a parabolic one with the same variance. Though the bunch shapes are different, their amplitudes in the spectra agree with each other within 5% when the normalized frequency $\omega\sigma_t$ is less than 1, where $\sigma_t$ is the RMS bunch length. Detecting two frequency components $(\omega_2 > \omega_1)$ of the beam spectrum under the condition $\omega\sigma_t < 1$, we have

$$\sigma_t = \sqrt{\frac{2}{\omega_2^2 - \omega_1^2} \ln \left\{ \frac{F_1(\omega_1)}{F_2(\omega_2)} \right\}}.$$

(5)

This is the same equation as that derived using a Gaussan disribution. Therefore, we can obtain the RMS bunch length by measuring the attenuation coefficient in the spectrum for any distribution function including asymmetric profiles.

Based on the considerations mentioned above, RMS bunch length monitors (BLMs) are developed for the both rings of KEKB. The bunch signal is picked up by a button electrode wiht 6 mm in diameter installed on the beampipe with an inner diameter of 64 mm. The lower frequency, $\omega_1$, is chosen to be $2\omega_{\rm rf}$ (1.0GHz) to avoid the noise appearing at the rf frequency $\omega_{\rm rf}$; the upper frequency, $\omega_2$, is chosen to be $5\omega_{\rm rf}$ (2.5GHz) to avoid the noise caused by wakefields propagating in the beampipe because the wavegide-mode cut-off frequency of the beampipe is estimated to be 2.7 GHz.

A block diagram of the detector is shown in Fig. 55. A beam signal from the button pickup is split into two channels, and then filtered by band-pass filters tuned at $\omega_1$ and $\omega_2$, respectively, with a 50 MHz-bandwidth to extract two frequency components. Each of the filtered siganals is mixed down to a common frequency of 70 MHz with a commercially available local oscillator, and detected by a synchronous detector. The frequency response of the synchronous detector is 1 kHz, which is roughly equal to the synchrotron frequency. The outputs of the two synchronous detectors corresponding to the spectrum amplitudes at $\omega_1$ and $\omega_2$, respectively, are fed to an analog calculator unit (ACU) where the bunch lenghth is calculated accoding to Eq. (5). Finally, the output of the ACU is read by a digital multimeter. The error in the bunch-length measurement is dominated by the imbalance of the two synchronous detectors ($\approx 0.3\%$) is estimated to be less than 10% for $\sigma_z \approx 6$mm, and is slightly enhanced for a small bunch length.
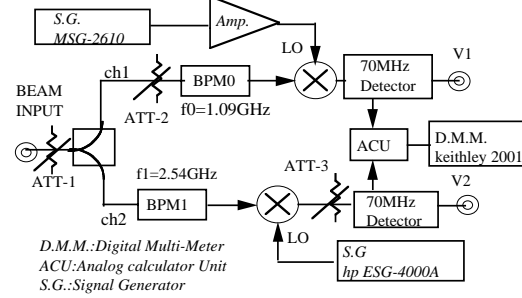


Fig. 55. Schematic diagram of the RMS bunch length monitor.

### 7.1.2 Measurements

Figure 56 shows an example of the measured bunch length as a function of the bunch current in the HER operated in a single-bunch-mode. The bunch length in the form of FWHM/2.354 was also meausred by the streak camera for a comparison. FWHM is the full-width at half maximum of the bunch profile measured by the streak camera and FWHM/2.354 corresponds to the RMS bunch length for the case of the Gaussian profile.

The difference between the RMS bunch length measured by the RMS BLM and the FWHM/2.354 by the streak camera is enhanced as the bunch current
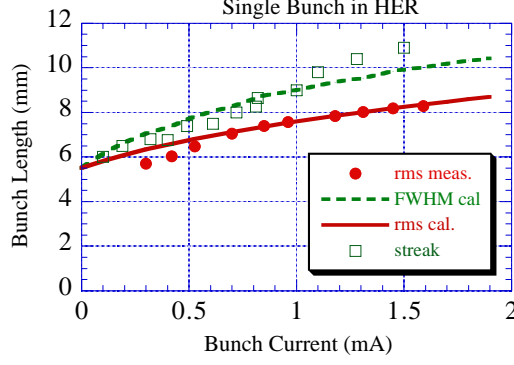
Fig. 56. Measured bunch lengths by the RMS BLM (dots) and the streak camera (squares), where the natural bunch length is 5.4mm. The BLM indicates RMS bunch length and a streak camera fwhm/2.354. Solid line (RMS) and broken line (fwhm/2.354) are calculated bunch lengths, assuming that $|Z/n| = 0.076\Omega$.
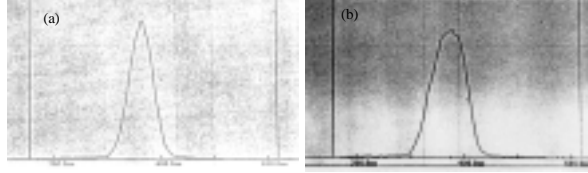


Fig. 57. Longitudinal profiles of a bunch measured by the streak camera at the bunch currents of (a) 0.2 mA and (b) 1.1 mA in the HER.

increases. To investigate this difference, we estimated the bunch lengthening with an inductive impedance model. The calculated RMS bunch length (solid line) and that expressed by FWHM/2.354 (broken line) shown in Fig. 56, assuming an inductive impedance of $|Z_i/n| = 0.076\Omega$, agree with the measured results of the RMS BLM and of the streak camera, respectively. This result indicates that we have a longitudinal impedance about 5 times larger than the design value of $|Z_i/n| = 0.015\Omega$; the difference between the measured results by the BLM and by the streak camera is caused by the fact that the bunch profile changes shape from a Gaussian-like profile to a parabolic-like profile as the bunch current increases, as shown in Fig. 57. Bunch lengthening in the LER is also observed, as shown in Fig. 58, where the solid line indicates the calculated bunch length with the assumption $|Z_i/n| = 0.072\Omega$. The LER impedance is expected to be 5-times larger than that of the design as well as that of the HER. This unexpected large impedance has affected the transverse impedance. The transverse mode-coupling instability was observed in the case of a low synchrotron tune [27].

Measurements of the bunch length averaged over the bunch train in a multi-bunch operation, depicted in Fig. 59, show that the bunch length as a function of the average bunch current is 0.27 mm/0.1 mA for the HER and 0.33 mm/0.1 mA for the LER, respectively. This result is almost independent of the filling pattern of bunches in the rings, and consistent with bunch
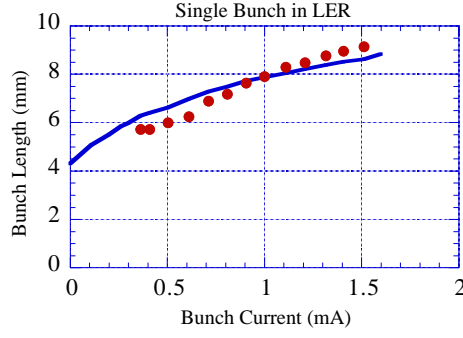
Fig. 58. Dots are measured bunch length, and the solid line indicates calculated bunch length, assuming that $|Z/n| = 0.072\Omega$. The natural bunch length is 4.3mm.

lengthening expected under single-bunch operation. An RMS BLM measurement has also confirmed no significant change in the bunch length for a 4 rf-bucket bunch spacing and for a 3 rf-bucket spacing.
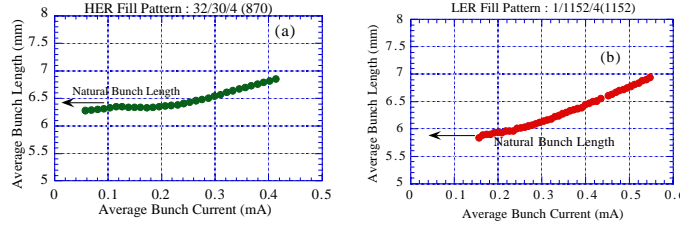


Fig. 59. The left graph shows average bunch-length vs. average bunch current in the HER with the number of bunches of 870. The natural bunch length is 6.4mm. The right shows average bunch-length in the LER, where the number of bunches is 1152. The natural bunch length is 5.8mm.

## 7.2 *Bunch-length measurements using a high-power rf waveguide system*

It may be possible to evaluate the bunch length from a spectrum measurement for the beam-indeced field in the rf cavity propagating in the waveguide, with a wideband pickup mounted on the waveguide of the rf system at the klystron gallery [8]. The frequency components with a frequency much higher than the waveguide cut-off frequency can propagate in the waveguide, and the spectrum deformation of the propagating field may be expected to be small in such a high-frequency region. The key point of this measurement is the choice of signal pickup with a flat response in the measurement band. Based on careful investigations on the pickup with MAFIA and a network-analyzer test bench, the small stripline pickup shown in Fig. 60 is designed for a wideband pickup with a flat response in the frequency range 5–40 GHz [8]. In order to avoid coupling with the high-power rf field, the stripline is installed parallel to the

microwave propagating direction so as to couple to neither the electric field nor to the magnetic field of the TE10 mode.
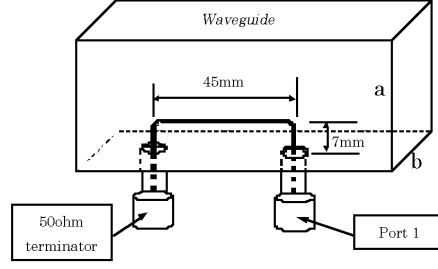


Fig. 60. A stripline type pickup mounted on the wall of high power rf waveguide system.

Figure 61 shows an example of the spectrum observed by a pickup for the LER. The fundamental mode of the rf is observed at 508.85MHz, and we have significant attenuation of the spectrum components induced by the beam in the frequency region below 5 GHz. On the contrary, above 5 GHz, since the wavelength of the field component is much smaller than the dimension of the waveguide, almost all of the components pass through the waveguide and are detected by the pickup. The bunch length is evaluated from the spectrum of the picked up signal in this frequency region.
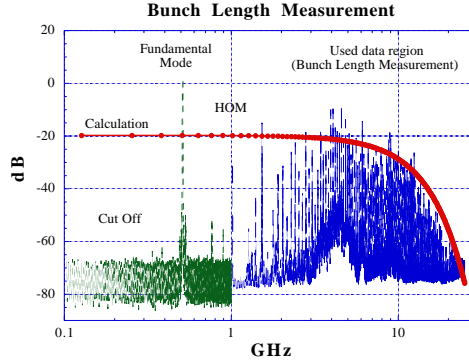


Fig. 61. Beam Spectrum measured in the LER through high power rf waveguide system and the spectrum of the Gaussian beam.

When a positron beam is filled in every 4th rf-bucket, the spectrum peak appears at every 127.22 MHz ($f_{rf}/4$) on the spectrum analyzer. The peaks between 5 GHz and 20 GHz are picked up and used to evaluate the bunch length. The picked-up spectrum data is fitted by a Gaussian profile with the fitting parameters of the bunch length and the normalization coefficient. The fitting result expects a bunch length of 8.04 mm as shown, in Fig. 62. This result is not far from other results obtained by a streak camera or an RMS BLM and demonstrates the possibility for applying this method to bunch-length measurements. However, we need to calibrate the un-known factor in

48

the response function to establish the system. Although it is very difficult to measure the response function of the cavity and the waveguide system, once the factor is calibrated by other measurements, such as a streak camera, we can determine the response function.
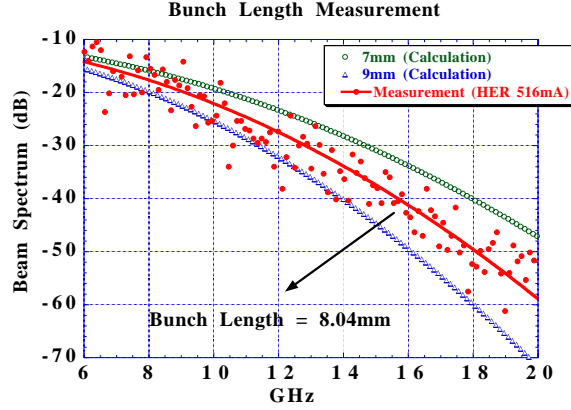


Fig. 62. Frequency components picked up every 127MHz (dots) and expected spectra for the bunch length.

It has been demonstrated that the bunch spectrum above the 5 GHz region can be observed by a pickup mounted on the waveguide of the rf system with only a small spectrum distortion where the spectrum distortion is much smaller than that observed by a button electrode through a coaxial cable. The vacuum-free installation of the pickup makes it possible to place a spectrum analyzer outside of the radiation area, and to easily modify the pickup and the read-out system for improving the system. This system is widely applicable to any accelerator. In addition to the bunch-length measurement, wideband signal detection is quite useful to observe various types of bunch oscillations.

## 8 Beam-loss monitors

To monitor beam losses during injection and storage of the KEKB accelerator, we initially installed 23 air ionization chambers in the Beam Transport (BT) Line and 109 chambers around the tunnel containing the electron and positron storage rings, forming part of the beam abort interlock system for machine protection. An additional 16 chambers dedicated to background studies were temporarily installed in the vicinity of the Belle physics detector. Recently, ion chambers near the movable masks have been replaced with PIN diode detectors for faster response.

## 8.1 Detector hardware

The free-air ionization chambers used were originally developed for use at the Proton Synchrotron [28]. The ion chamber is Fujikura FC-20D co-axial cable (See Fig. 63). The inner and outer conductors are separated by an air gap. Electrons freed by ionizing radiation are pulled toward the outer conductor, which is held at a positive potential of 200 V relative to the shield layer; the inner conductor collects positive ions, with a typical drift time of 1 ms. The resulting current is fed into an integrator/amplifier module, described in the next section. A spiral polyethylene spacer wraps around the inner conducter, permitting free air flow through the chamber.
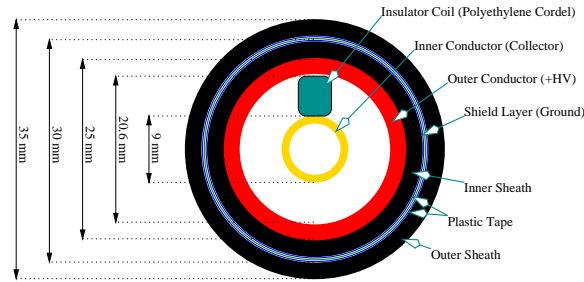


Fig. 63. Cross-section of ion chamber.

The effective threshold for ionizing radiation to penetrate into the chamber is about 1 MeV for electrons, and about 50 keV for $\gamma$ rays. Since at 200V there is no charge multiplication effect, the response of the chamber is determined from the volume of air enclosed between the outer conductor and the collector. For the FC-20D, this corresponds to $8.54 \times 10^{-8}$ C/R, or $9.74 \times 10^{-8}$ C/rad, per meter length of the chamber. The chambers around the KEKB ring tunnel consist of 5-meter long segments, with 16 1-meter segments for background studies placed around the beampipe near Belle, and 23 chambers of lengths ranging from 5 meters to 8 meters plus some doubled 5-meter-long segments in the BT line.

## 8.2 Ring chambers

The purpose of the ring chambers is to monitor beam losses during injection, and to provide machine protection in the event of a sudden beam instability or loss. Figure 64 shows a block diagram of the loss monitor front-end electronics for a chamber in the KEKB ring. The 5-meter long chambers in the ring are mounted on the outer wall of the tunnel near the beampipe, and are distributed roughly evenly around the ring with an average spacing of 28 meters per chamber. Each chamber is connected to an electronics rack in one of four sub-control rooms located around the ring. A low-pass filter is attached

to the supply voltage input near the chamber to block pick-up noise and to provide a current-limiting resistance in the event of a break-down.
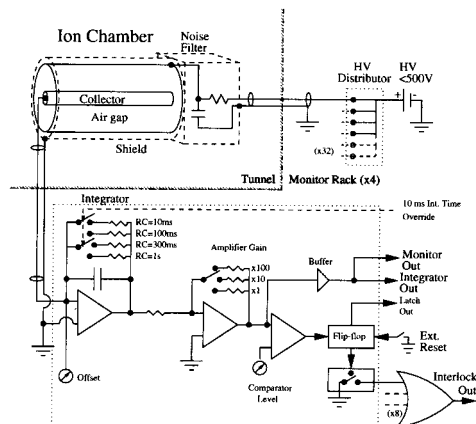


Fig. 64. Block diagram of the beam-loss monitor front-end electronincs.

The front-end module consists of three stages: integrator, amplifier, and comparator/latch. Each module handles eight channels, with four modules per quadrant. In the first stage, a 47 nF integrating capacitor gives 10.2 mV/mrad for the 5 meter chambers in the ring. The RC time constant is selectable at 4 settings of 10, 100, 300, or 1000 ms; amplifier gains of 1, 10 and 100 are selected via front-panel switches or remote-control.

A comparator is used to issue a hardware beam-abort signal if the loss level exceeds a threshold which is settable for each channel by a front-panel potentiometer. The latches for all 8 channels in the module are OR'ed together to form the abort interlock signal.

In parallel with the comparator stage, the loss signal is buffered and sent to a 16-bit ADC (Profort PVME-332). In the stored-beam mode, the ADC is sampled at 1-second intervals using an internal timer inside the VME controller, with the integrator time constant set to 1 second. During beam injection, the integrating time constant is chosen to be 10 ms, which is half the width of the injection cycle at the maximum injection rate of 50 Hz. In this mode, the ADC sampling trigger is synchronized to the injection trigger, but delayed 1.4 ms to match the peak of the loss signal after injection due to the drift time in the chamber. The rise time of the pulse is largely determined by the drift time of the chamber, and the fall time by the integrator time constant.

The data-acquisition and control system for the loss monitors is based on the EPICS IOC system in use at KEKB. The ADCs and digital I/O units are mounted in VME crates, one in each sub-control room, from which readings are relayed once per second to a loss-monitor display panel running in the control room; it can also be logged separately. A typical example of the display is shown in Fig. 65.
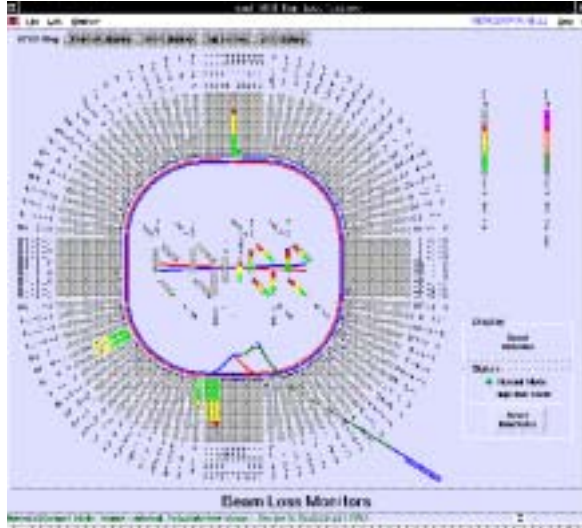
51

Fig. 65. Diplay of beam-loss monitors.

*8.3  Beam transport line*

A variant of the ring loss-monitor system was installed in the Beam Transport (BT) line which connects the end of the linac with the KEKB rings. The integration period is adjustable by front-panel control of the clock generator in a separate control module, ranging from 0.2 to 3.2 seconds in units of 0.2 seconds. The value at the end of the integration period is held in the sample-hold buffer of the comparator module, and is read out via a CAMAC-based ADC. The comparator can be used to open an interlock line for the radiation safety system; 8 of the 23 channels in the BT line are connected to a radiation-safety interlock system.

*8.4  PIN diode detectors*

At high beam intensities some of the movable masks have suffered excessive damage from beam impact on the mask face when rapid orbit changes occur. In order to protect the masks from such rapid beam-orbit changes, it was determined to replace the slow-response ion chambers near the masks with detectors capable of triggering a beam abort within a few beam revolutions (10 $\mu$sec/revolution). For this purpose, PIN diodes have been deployed around the masks. The rise time of the beam-loss signal from the PIN diodes is essentially determined by the capacitance of the signal cable (30 nF for a 400-m cable) and an input impedance of 2 k$\Omega$, having a time constant of 60 $\mu$sec. A preamplifier stage incorporating a track-and-hold is used to integrate the signal before it is fed to the programmable amplification second stage, which is modified from the ion-chamber modules. The track-and-hold signal output preserves

52

the rising-edge time constant of the input signal from the PIN diodes, with a falling-edge time constant of 3 msec. A block diagram of the preamplifier is shown in Fig. 66.
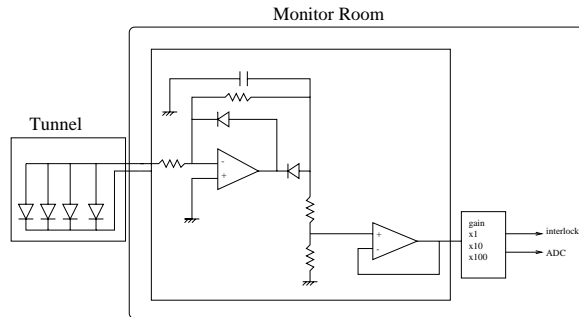


Fig. 66. Block diagram of pre-amplifier for PIN diode loss monitors

In tests in the spring of 2001, the PIN diode system was found to be capable of detecting beam losses within a few revolutions. Following these tests, a full set of 8 PIN diodes at each of the 24 mask locations in the LER and HER rings has been installed for use from autumn 2001.

## 9    Summary

The effective bandwidth of the BPM system for a closed-orbit measurement of the KEKB rings is widely programmable, and it is easy to optimize the measuring time and accuracy for the various operation modes of the rings. The resolutions of the BPMs were estimated to be 2-4$\mu$m by a 3-BPM correlation method, where the actual resolution is expected to be better than the measured one, since the measurement includes errors due to small orbit oscillations. The center offset of each BPM was corrected by a beam-based alignment with a typical accuracy of about 40$\mu$m. The CODs of both rings are continuously measured every 2-3 sec and corrected every 20-30 seconds based on the BPM data. To keep the collision condition stable, the position offset of the interaction point and the crossing angle of the electron and positron beams are automatically controlled using 4 BPMs in the interaction region. To complement these BPMs, special BPMs with 8 button electrodes are also installed at the front end of the superconducting quadrupole magnets for the final focusing, where the positron and the electron beams pass through together in the BPMs. To obtain each beam position separately from the composite signal, an algorithm based on the nonlinearity of the BPM detector was developed and tested. These special BPMs will be in operation soon.

A new type of the BPM which can detect transverse and longitudinal positions, in turn-by-turn, in addition to the charge of a bunch based on parameters represented in four dimensions has been developed for the KEKB rings. An RMS

transverse position resolution of 20 $\mu$m has been obtained for bunches in actual beams. The minimum detectable intensity corresponds to a beam charge of 50 pC, or a bunch current of 5 $\mu$A. The monitor can distinguish between an energy error and a phase error of an injected beam. The circumference of the HER was determined by measuring the injected beam phase, turn-by-turn. The monitor is efficiently used for beam-dynamics experiments, such as damp of the betatron oscillation and the measurement of loss factors. Moreover, bunch-by-bunch phase has been measured along a bunch train with a resolution of degrees by attaching a gate module to the turn-by-turn monitor.

New beam DCCTs with parallel feedback circuits have been developed for KEKB to overcome a difficulty in selecting a balanced magnetic core for parametric flux modulation. The parallel feedback DCCT makes it possible to employ a non-selected pair of magnetic cores for parametric modulation and to successfully suppress any residual modulation ripple noise to the order of $\mu$A in spite of a wideband response.

The transverse bunch-by-bunch feedback systems for the KEKB rings have been greatly contributing to both the commissioning of the rings and the operation of the colliding experiment from early stages of the commissioning up to the present, representing about 2.5 years of operation. A damping time of around 0.2 ms (20 turns) has been achieved under stable operation of the feedback systems. The feedback systems have successfully suppressed the instabilities in both rings under a high-current operation exceeding 900 mA in the LER and 800 mA in the HER. Experiments concerning special filling patterns suggest the existence of a large impedance source in the ring. The feedback systems and the analysis tools, such as the BOR with transient-domain analysis, or the beam loss trigger, will continue to play important roles to increase the luminosity of KEKB.

Continuous tune measurements by the gated tune meter is indispensable not only for a delicate manipulation of the betatron tune, but also for investigations on the photo-electron cloud density and trapped-ion problems in KEKB.

Optical beam-diagnostic systems using streak cameras, fast-gated CCD cameras and SR interferometers have been installed in the KEKB rings. An online SR interferometry analysis system for the beam-size measurements is developed and it is working well to deliver real-time measurements of the beam size continuously, where the error due to any surface deformation of the SR extraction mirror is automatically compensated by fitting the fringe pattern with independent diffraction patterns of two slits. This algorithm makes us free from any mirror deformation problems. Machine studies, such as vertical beam size blow-up, caused by a photo-electron cloud in the LER etc. are very actively performed using the optical diagnostic system. The system has been successfully operating and has greatly improved the efficiency of the KEKB

commissioning.

Bunch length measurements by the RMS bunch-length monitor give consistent results with that of streak-camera measurements. We have found from the bunch lengthening that the measured impedance is about 5-times as large as the design value in both rings. The measured bunch lengths in both rings show that the averaged bunch length during multibunch operation with a 4-rf-bucket spacing roughly agrees with that in single-bunch operation. A wideband stripline pickup is also mounted on the wall of high-power rf waveguide between the klystron and the rf cavity to observe the frequency spectrum of the beam in the range from 5 GHz to 20 GHz. It has been demonstrated that this type of pickup is usefull to measure the average bunch length and to detect the longitudinal coherent motion of bunches.

To monitor beam losses, air-ionization chambers made from air-insulation coaxial cables are distributed along the beam-transport line and around the KEKB rings. These form a part of the beam-interlock system for machine protection. For protecting the beam masks from beam impact, the slow-response ion chambers at the 24 mask locations have been replaced by PIN diodes to serve as a trigger signal for the interlock system within a few beam revolutions for use from the next commissioning of KEKB.

## Acknowledgements

## References

[1]  KEK Report 95-7.

[2]  T. Ieiri and T. Kawamoto, Proc. 11th Symposium on Accelerator Science and Technology, Harima, Japan (1997) 412.

[3]  T. Ieiri and T. Kawamoto, NIM A 440 (2000) 330.

[4]  M. Tobiyama and E. Kikutani, Phys. Rev. ST Accl. Beams 3,012801(2000).

[5] M. Tobiyama et al., in Proceedings of 12th Symp. Accel. Sci. and Tech, Wako, Saitama, Japan (1999) p.555.

[6] S. Hiramatsu and M. Arinaga, Proc. 12th Symposium on Accelerator Science and Technology, Wako, Japan, 1999, pp.561-563.

[7] T. Ieiri, Measurement of Bunch Length based on Beam spectrum in KEKB, EPAC2000, Vienna, Austria (2000).

[8] T. Mimashi et al., Bunch Length Measurement and the Beam Signal Observation through High Power RF Waveguide System, to be published in Proc. of the 18th Int. Conf. on High Energy Accelerators, Tsukuba, Japan (2001).

[9] T. Obina, et al., Damped Button Electrode for B-Factory BPM System,Dallas, Texas, U.S.A.

[10] T. Katoh, et al., ICALEPCS97, Beijing, China.

[11] M. Masuzawa, et al., Proc. EPAC2000, Wien, Austria.

[12] H. Fukuma, private communications.

[13] N. Akasaka, private communications.

[14] Y. Funakoshi, et al., "Feasibility Study of an Orbit Feedback System for the KEKB Facility", Proc.PAC95

[15] K. Satoh, "Detection of the position of two beams with a common BPM", Proc. PAC99

[16] K. B. Unser, IEEE Trans. on Nucl. Sci., NS-16, 1969, pp.934-938.

[17] K. B. Unser, IEEE Trans. Nucl. Sci., NS-28, No. 3, 1981, pp.2344-2346.

[18] K. B. Unser, Proc. 1991 Accelerator Instrumentation Warkshop, CEBAF, 1991; AIP Conf. Proc. No. 252, 1992, pp.226-275. (CERN SL/91-42 (BI), 1991)

[19] H. Koiso, private communication.

[20] T. Ieiri et al., to be published in Proc. of the 18th Int. Conf. on High Energy Accelerators, Tsukuba, Japan (2001).

[21] J.W. Flanagan, S. Hiramatsu and T. Mitsuhashi, EPAC2000, Vienna, Austria (2000), p. 1714.

[22] T. Mitsuhashi, N. Takeuchi, S. Hiramatsu, M. Itoh and T. Yatagai, Proc. APAC98, p698,(1998).

[23] J.W. Flanagan, T. Mitsuhashi and S. Hiramatsu, Proc. PAC99, p.2120,(1999).

[24] T. Mitsuhashi, Beam Profile and Size Measurement by SR Interferometers : Beam Measurement, Ed. by S. Kurokawa et al., pp399-427, World Scientific,(1999).

[25] J.W. Flanagan, H. Fukuma, N. Akasaka, S. Hiramatsu, T. Mitsuhashi and K. Oide, EPAC2000, Vienna, Austria (2000), p. 1119.

[26] W.H. Press, S.A. Teukolsky, W.T. Vetterling and B.P. Flannery, *Numerical Recipes in C: The Art of Scientific Computing*, Second Edition, CUP (1992) pp. 681-688.

[27] T. Ieiri et al., EPAC2000, Vienna, Austria (2000), p. 1423.

[28] H. Nakagawa, S. Shibata, S. Hiramatsu, K. Uchino and T. Takashima, NIM 174 (1980) p. 401.